NASA TECHNICAL NOTE

NASA TN D-7925

NASA TN D-7925

A TWO-PARAMETER SCINTILLATION SPECTROMETER SYSTEM FOR MEASUREMENT OF SECONDARY PROTON, DEUTERON, AND TRITON DISTRIBUTIONS FROM MATERIALS UNDER 558-MeV-PROTON IRRADIATION

Sherwin M. Beck

Langley Research Center
Hampton, Va. 23665

NATIONAL AERONAUTICS AND SPACE ADMINISTRATION • WASHINGTON, D. C. • OCTOBER 1975

1. Report No. NASA TN D-7925	2. Government Accession No.	3. Recipient's Catalog No.
4. Title and Subtitle A TWO-PARAMETER SCINTILLATION SPECTROMETER SYSTEM FOR MEASUREMENT OF SECONDARY PROTON, DEUTERON, AND TRITON DISTRIBUTIONS FROM MATERIALS UNDER 558-MeV-PROTON IRRADIATION		5. Report Date October 1975
		6. Performing Organization Code
7. Author(s) Sherwin M. Beck		8. Performing Organization Report No. L-9941
		10. Work Unit No. 506-16-35-01
9. Performing Organization Name and Address NASA Langley Research Center Hampton, Va. 23665		11. Contract or Grant No.
		13. Type of Report and Period Covered Technical Note
12. Sponsoring Agency Name and Address National Aeronautics and Space Administration Washington, D.C. 20546		14. Sponsoring Agency Code
15. Supplementary Notes		

16. Abstract

A two-parameter scintillation spectrometer system has been developed and used to obtain proton, deuteron, and triton double differential cross sections from materials under 558-MeV-proton irradiation. The system measures both the time of flight of secondary particles over a 488-cm flight path and the energy deposited in a scintillator, 12.7 cm in diameter and 30.48 cm long. The time resolution of the system is 0.39 nsec. The calculated energy resolution based on this time resolution varies with energy from 1.6 percent to 7.75 percent for 50- and 558-MeV protons, respectively.

The system and its performance are described in detail. Various systematic and statistical errors are evaluated, and the double differential cross sections for secondary proton and deuteron production at 20° from a 2.35 g/cm^2 thick beryllium target are shown as an example of the results obtainable with this system. The uncertainty in the cross sections for secondary protons varies with particle energy from approximately ±9 percent at 50 MeV to approximately ±11 percent at 558 MeV.

17. Key Words (Suggested by Author(s)) Protons Deuterons Cross sections Spectrometer		18. Distribution Statement Unclassified — Unlimited Subject Category 73	
19. Security Classif. (of this report) Unclassified	20. Security Classif. (of this page) Unclassified	21. No. of Pages 62	22. Price* $4.25

*For sale by the National Technical Information Service, Springfield, Virginia 22161

CONTENTS

A TWO-PARAMETER SCINTILLATION SPECTROMETER SYSTEM FOR MEASUREMENT OF SECONDARY PROTON, DEUTERON, AND TRITON DISTRIBUTIONS FROM MATERIALS UNDER 558-MeV-PROTON IRRADIATION

Sherwin M. Beck
Langley Research Center

SUMMARY

A two-parameter scintillation spectrometer system has been developed and used to obtain proton, deuteron, and triton double differential cross sections from materials under 558-MeV-proton irradiation. The system measures both the time of flight of secondary particles over a 488-cm flight path and the energy deposited in a scintillator, 12.7 cm in diameter and 30.48 cm long. The time resolution of the system is 0.39 nsec. The calculated energy resolution based on this time resolution varies with energy from 1.6 percent to 7.75 percent for 50- and 558-MeV protons, respectively.

The system and its performance are described in detail. Various systematic and statistical errors are evaluated, and the double differential cross sections for secondary proton and deuteron production at 20° from a 2.35 g/cm^2 thick beryllium target are shown as an example of the results obtainable with this system. The uncertainty in the cross sections for secondary protons varies with particle energy from approximately ±9 percent at 50 MeV to approximately ±11 percent at 558 MeV.

INTRODUCTION

This report describes a two-parameter spectrometer system developed and used in an experimental program to obtain double differential cross sections for the production of secondary charged particles from materials bombarded by protons at energies found in the near-Earth radiation environment. This system was used at the NASA Space Radiation Effects Laboratory (SREL) to measure the energy and angular distributions of secondary protons, deuterons, and tritons from a number of elemental materials at laboratory angles from 10° to 60°. The system and its performance are described, and in addition, details of error evaluation and data analysis are presented. The double differential cross sections for proton and deuteron production at 20° in a 2.35 g/cm^2 thick beryllium target irradiated with 558-MeV protons are given as an example of the results obtainable with this system. The system was designed to be assembled by two men within a normal 8 hour working day and to be operated by one man thereafter. The experimental setup can be dismantled within 2 hours by two men. This ease of handling maximized the use of allotted beam time at SREL.

Studies of neutrons and charged particles with energies up to several GeV have been performed with the time-of-flight technique. (See refs. 1 to 8.) Generally, neutron measurements involve flight paths of tens of meters, whereas the charged particle studies have used much shorter distances. Because the velocity resolution is inversely proportional to the flight path, the longest path possible is desired. However, the longer the flight path, the greater the importance of particle scattering by the intervening atmosphere and the greater the running time required to accumulate data because of the reduced solid angle. The measurement of flight times over the flight path requires a time fiducial, usually derived from the accelerator beam or radio frequency (rf) system, and a second timing signal, obtained from a detector, which defines the end of flight.

The size of the detection system described in this report was limited by the dimensions of the SREL proton target area to a maximum flight path of 6 m for a maximum angle of 60°. In addition, the width of the proton beam microburst was approximately 10 nsec which required that the timing fiducial be derived from the scattered particles rather than from the incident proton beam or the cyclotron rf system.

The spectrometer measures the flight time over a 488-cm path and the kinetic energy deposited in a plastic scintillator, 12.7 cm in diameter and 30.48 cm long. From these two measured parameters the mass of secondary particles is determined. The kinetic energy of secondary particles is calculated from the flight time and particle mass.

The time-of-flight technique was chosen for this experimental program because it would provide good data without the expense and manpower involved in the design and use of a magnetic momentum analyzing system.

SYMBOLS

A	cross-sectional area of target active volume viewed along the detection system center line
b	base leg of equilateral triangle defined by ϕ and R, cm
c	speed of light in vacuum, 2.997925×10^{10} cm/sec
d	distance between detector sets, 488 cm

E_5	linear signal from detector 5
F	frequency of proton beam macroburst, Hz
f	cyclotron oscillator frequency, Hz
K	particle kinetic energy, MeV
K'	particle kinetic energy measured by time-of-flight system, MeV
K_o	initial kinetic energy of secondary particle produced in target, MeV
$d\ell$	element of length along S
m	particle rest mass, kg
N	number of particles intercepting detector sets 1 and 2 with no scatting from detector set 1
N'	number of particles intercepting detector sets 1 and 2 with multiple scatting in detector set 1
R	distance from detector bench pivot point to end of bench, cm
r	cross-sectional radius of incident proton beam
S	distance traveled by particle in system
T	duration of proton beam macroburst, sec
t	duration of proton beam microburst, sec
t_d	dead time, sec
t_f	time of flight over distance d, sec
W	weighting factor used in solid-angle calculations

w	width of target cross section as viewed along center line of detection system
x,y,z	rectangular coordinates
ΔK	energy difference
$\Delta K/K$	energy resolution
Δt_{beam}	time spread corresponding to energy spread in incident proton beam
Δt_f	time spread at full width at half maximum of incident proton beam measured by the time-of-flight system
Δt_{sys}	time resolution of detection system
σ	standard deviation of Gaussian curve
τ	thickness of target
ϕ	angle between proton beam center line and center line of detection system, deg

Abbreviations:

ADC	analog-to-digital converter
CFTD	constant fraction timing discriminator
diam	diameter
FWHM	full width at half maximum
TOF	time of flight
TPHC	time-to-pulse-height converter

Subscripts:

A	air
Al	aluminum
He	helium
s	scintillator
t	target

APPARATUS

Detectors

The components of the time-of-flight and energy spectrometer are identified in figure 1, and the more important features of the apparatus are discussed in detail. The housings for detector sets 1 and 2 each contain two separate photomultiplier tube and scintillator assemblies (two detectors). The entrance and exit windows each consist of two sheets of 0.00064-cm-thick aluminized polyethylene terephthalate. The exit window of the first housing and the entrance window of the second one are seals for the helium-filled gas bag. The interior of each housing was sprayed with a flat black paint to minimize the effects of any light leaks.

The scintillation plastic used for the detectors is a patented combination of p-terphenyl and p,p′-diphenylstilbene. The scintillation properties of this material were given as 68-percent light output relative to anthracene, decay time of 1.7 nsec, peak fluorescence wavelength of 408 nm, and light transmission of 154.9 cm (distance to reduce intensity to one-half the initial value). The plastic was obtained in both sheet and rod form. The large cylindrical scintillator for detector 5 (12.7 cm in diameter and 30.48 cm long) was supplied on special order. Severe surface crazing developed on the thin scintillators after approximately 6 months, and they were replaced. However, the large scintillator has been used over a period of 3 years without serious surface degradation.

The mounting configurations for detectors 1 to 4 used in the spectrometer are shown in figure 2, and the thickness of each scintillator is given in table I. A silicone grease was used to increase the optical coupling between the scintillators and the photomultiplier tubes. A reflective cover of 0.00254-cm-thick aluminum foil was used on all surfaces of the rectangular scintillators except the edge in contact with the photomultiplier tube, and on only the upper edge of circular detector 2. The same thickness of aluminum foil was used to cover all surfaces of detector 5 except the end in contact with the photomultiplier tube.

Photomultiplier Tubes

The photomultiplier tubes were selected primarily for high current gain and fast rise time. All tubes were obtained from the same manufacturer; however, no attempt was made to match the gains. Tubes used for detectors 1, 2, 3, and 4 had a useful photocathode diameter of 42 mm, gain at 2500 V of 10^8, rise time of less than 1.8 nsec, anode linearity up to 300 mA, and spectral response of type A (S11). The output impedance of all tubes was 50 Ω. The anode pulse shapes were nearly Gaussian with a full width at half maximum of less than 3.5 nsec and a base line overshoot of less than 5 percent.

The photomultiplier tube bases which contain the voltage divider circuits were obtained from the same manufacturer as the tubes. The voltage divider network in each base was adjusted to give the greatest anode output and best waveform when a scintillator, 2.54 cm in diameter and 2.54 cm long, was mounted on the tube and irradiated with Co^{60} gamma rays.

The large photomultiplier tube for detector 5 had a stated current gain of 10^8 at 2400 V, rise time of 2 nsec, full width at half maximum of 3 nsec, and anode linearity up to 300 mA. The minimum useful diameter of the photocathode was 110 mm. The spectral response was type A (S11). With the large scintillator mounted on the tube, the voltage divider network in the tube base was adjusted to give the best pulse height and waveform at 2400 V with the scintillator exposed to a 10-μCi Co^{60} source.

Proton Beam Characteristics

The beam transport system of the NASA Space Radiation Effects Laboratory (SREL) is shown in figure 3. This system was designed and constructed to provide particle beams at a height of 137.16 cm above the floor. The length of the transport system from the cyclotron to the proton target area is approximately 51.82 m. There are 20 quadrupoles and 5 bending magnets which can be used to transport the beam to the proton target area. By using all elements of the system, very intense beams of protons can be delivered to the proton target area; however, it was very difficult to obtain both a small beam spot and a parallel beam when all elements of the system were used. Through trial and error it was found that a nearly parallel beam less than 2.54 cm in diameter could be obtained by turning off certain elements in the transport system and by inserting a collimator before quadrupole Q17. The elements of the system used for the measurements discussed in this report are shown in figure 3 with shading.

The collimator before Q17 was a 20.32-cm-thick lead block with a 1.27-cm-diameter hole drilled through the block. Quadrupoles Q21 and Q22 were operated at a low power level and were used only to "fine tune" the beam spot at the target position. The position of the beam spot is strongly dependent on the current in bending magnet M7 because of the 13.10-m level arm at the target and the low power settings of Q21 and Q22. Because the power supplies for the elements in the transport system are very stable, the position of the beam spot center at the target position did not vary more than 0.5 cm during any 24 hour period.

The beam spot diameter and beam divergence were obtained by measuring the diameter of the beam image on fast photographic film placed at the target position and at a point 6 m from the target position. The film was exposed for approximately 5 sec at maximum beam intensity. The images at both positions were sharp and nearly circular. The beam image at the target position was 2.6 cm in diameter and the second image 6 m away was approximately 4.5 cm in diameter. The beam image at various points behind the target position steadily increased in size with increasing distance from the target. This indicated that the beam was focused at or in front of the target. The beam divergence angle was then calculated to be 0.003 rad.

The extracted proton beam from the SREL cyclotron is modulated on both a macroscale and a microscale as shown in figure 4. The time structure of the extracted beam was obtained with a Čerenkov radiator placed in the direct beam. The detector was a 2.54- by 0.6- by 10.16-cm piece of nonscintillating plastic mounted on a fast-rise-time photomultiplier tube which had a 4-nsec anode pulse width at half maximum. The anode signal was fed to a fast sampling scope, and the resulting display was photographed. The observed width of the microbursts was approximately 9 nsec. After removing the instrument width, the true width of the microbursts is approximately 8 nsec. The duration T of the macroburst varied with beam intensity from approximately 20 to 110 μsec, and the bursts were produced at a frequency F near 55 Hz. The microbursts occur at a frequency determined by the frequency of the cyclotron oscillator which was set at $f = 17.42$ MHz for these measurements. The time between bursts is

$$1/f = 57.4 \text{ nsec}$$

Alinement of Detectors

As stated previously the beam transport system of SREL was designed and constructed to provide protons at a height of 137.16 cm above the floor. However, because of changes in the transport system and settling of the building, the beam height in the proton target area has slowly increased. At the time of these measurements the beam height was determined to be 138.43 cm above the floor. Because of uncertainty in the beam height, the following procedure was used each time the detection system was reassembled.

The center of the target table was placed approximately 175 cm from the exit window of the transport system and directly under the expected position of the beam. The target holder was next mounted on the table, and a small frame containing a set of crosshairs was clamped to the holder with the center of the crosshairs at the expected beam position. A second frame and crosshair set were located 8 m from the target table at approximately the beam position. A reference pressure mark was made on each of two sheets of fast photographic film, and the film was then placed in the frames with the reference marks alined with the crosshairs. The film was exposed to the proton beam for approximately 5 sec and developed. The displacement of the beam spot from the reference mark was noted, and the two frames were moved to position the crosshairs in the center of the beam. A second set of film was exposed to ensure that the crosshairs were correctly positioned. A 1-mW helium-neon laser was placed between the exit window of the transport system and the target table and alined with the two sets of crosshairs. The laser beam was then used as the reference for system alinement.

The detector bench was connected to the pivot, and the bench track was checked for proper horizontal alinement. The large scintillation detector 5 was attached to the rear platform of the bench. The height of the track was changed, if necessary, to make the long axis of the detector coaxial with the beam line defined by the laser. Detector 4 was next positioned with the laser beam at the center of the scintillator. Detectors 3, 2, and 1 were sequentially positioned, and the enclosures for the detectors were bolted in place. Next, the target holder was mounted on the target table and clamped in position. Reference marks were made on the frame of the holder to indicate the position of the beam center. Finally, the laser was removed and the ion chamber was put in position. The second frame and crosshair set were left in place and were used periodically to check the position of the beam.

Detector Bench

The detector bench shown in figure 1 was of open, rectangular, box-frame construction. The cross-sectional dimensions were approximately 21 by 56 cm, and the overall length was approximately 700 cm. The bench was connected to the target table by a movable collar. The weight of the bench at the end away from the target was carried by two swivel casters which rolled on the horizontal track.

The enclosures for detector sets 1 and 2 and large detector 5 were bolted to the bench to maintain system alinement. As part of the alinement procedures the longitudinal axis of detector 5 was placed directly above the center line of the bench. The bench center line was then used for angular positioning of the detection system.

The angular positioning of the detector bench was done by triangulation. By using the distance $R = 682$ cm from the pivot point located at the center of the target table to the point at the rear of the bench on the bench center line, the displacement b of the reference point from the vertical plane containing the proton beam ($\phi = 0^\circ$) for a given angle ϕ is

$$b = 2R \sin (\phi/2)$$

The accuracy of the bench displacement was well within ±0.5 cm. The angular accuracy was then ±0.04°.

Arrangement of Electronic Equipment

All logic units (discriminators, coincidence units, and gate generators) conformed to signal requirements set forth in reference 9. The arrangement of electronic equipment shown schematically in figure 5 was the result of several tests to improve the flight-time and energy resolution, to decrease the system dead time, and to set time and sequence requirements between fast logic signals and slow linear signals to eliminate events produced by background radiation. The system can be considered as four subsystems interconnected by coincidence units.

The four subsystems are (1) fast logic, (2) time, (3) energy, and (4) parameter storage. The fast logic subsystem contains discriminators 1 to 5 and coincidence units (12), (345), and (12345). The components of the time subsystem are the two constant fraction timing discriminators (CFTD), the time-to-pulse-height converter (TPHC), the gate generator to the TPHC, and the bias and delay amplifiers. The energy subsystem contains the linear gate and stretcher module, bias amplifier, and delay amplifier. The parameter storage subsystem includes the two 128-channel analog-to-digital converters (ADC), the gate generator between the two, the two-parameter analyzer, and the magnetic tape system.

The energy and time subsystems are tied together at the lowest time sequence level by the output from the (345) coincidence unit in the fast logic subsystem. This interconnection ensures time coincidence between detectors 3, 4, and 5, signal input to the linear gate and stretcher module, and signal input to the start channel of the TPHC. The fast logic and energy subsystems are again tied together at an intermediate time sequence level by the $\left(12345 + E_5\right)$ coincidence unit. This coincidence requires that the "energy" output from the linear gate and stretcher module occurs from the same event that satisfied the fast logic subsystem. At the highest level of coincidence the (12345 + E_5 + TPHC) coincidence unit ties the fast logic, time, and energy subsystems to the parameter storage subsystem and ensures that all subsystems are satisfied by the same particle traversing the system.

For each particle traversing all five detectors in the system, the following events occur. Anode signals from detectors 2 and 4 are split with one-half of each signal going to one of two CFTD's (ref. 10) located approximately 2 m from the detectors. The other half-amplitude signals are sent to fast discriminators 2 and 4 in the readout area of SREL via approximately 45 m of RG-213/U coaxial cable. Anode signals from detectors 1, 3, and 5 are fed to discriminators 1, 3, and 5 in the readout room via RG-213/U cable. Outputs from discriminators 3, 4, and 5 are tested for time coincidence, and if all three signals overlap, a 50-nsec-wide output signal (345) triggers a gate generator which in turn gates "on" the start channel of the TPHC to accept a delayed signal from CFTD 4 connected to detector 4. A timing signal from CFTD 2 has been delayed with respect to timing signal 4 and fed to the stop channel of the TPHC. If timing signal 2 occurs within 45 nsec of signal 4, then the TPHC puts out a signal whose amplitude is proportional to the time difference between input signals. A simultaneous output signal (345) is also fed, along with coincident output signal (12), to another coincidence unit to test for overlap of all five signals.

Dynode signal (E_5) from detector 5 is delayed to permit time coincidence with output signal (345). The dynode signal is inverted and fed to a linear gate and pulse stretcher unit for amplification. The signal (345) is used to open the gate for the dynode signal. The linear gate and stretcher unit was set for a fixed dead time of 30 μsec after each output signal (E_5). For each output (E_5), a pulse is generated and fed to a coincidence unit along with a (12345) output to check time coincidence between signals. This (12345 + E_5) signal and the (TPHC) signal are tested at the highest level of coincidence. The (12345 + E_5 + TPHC) signal initiates a gate signal to the ADC's in the two-parameter analyzer system. The linear signals (TPHC) and (E_5) are processed through bias amplifiers to adjust the pulse amplitudes to meet the requirements of the ADC's; and the signals are delayed through delay amplifiers to match the (TPHC) and (E_5) signals with the gate signal.

The initial time alinement of the complete system requires from 2 to 3 hours. The detection system is first moved to the 0° position, and quadrupoles Q15 and Q16 in the transport system are defocused to spread the proton beam over a wide area of the collimator. Next, the bending magnet M7 is turned off to prevent any protons from passing through the detector system. After a low-level beam is established in the cyclotron, the transport beam stop is opened and the power to M7 is slowly increased to its operating level. If the count rate in detector 1 was greater than 100 counts per second, either the cyclotron internal beam current was reduced or Q15 and Q16 were further defocused.

A 250-MHz real-time dual-beam oscilloscope was used in the alternate channel mode to observe the relative time delay between two signals. Input signals to coincidence unit (12) were first compared, and either signal 1 or 2 was delayed to reduce the relative time difference at the coincidence unit to 0.5 nsec or less. Then the relative time difference between signals 3, 4, and 5 was also reduced to 0.5 nsec or less by comparing the signals two at a time. The output pulse width of coincidence (345) is set at 55 nsec and fed to the (12345) coincidence unit. Although particles pass through detectors 1 and 2 before reaching detectors 3, 4, and 5, the coincidence signal (12) is delayed until it just overlaps the trailing edge of the (345) signal. The (345) signal is then used to gate on the start channel of the TPHC. Next, output signal (TPHC) is delayed until the time difference between the start and stop signals is approximately 45 nsec. This method of operating the TPHC has two advantages: (1) the number of false starts by the TPHC is greatly reduced, since the coincidence (345) rate and also the CFTD 2 rate are always lower than the (12) rate by virture of a smaller solid angle; and (2) this reversed time scale permits the display of higher energy particles with larger pulse heights from the TPHC.

The time difference between pairs of inputs signals to the remaining coincidence units is also reduced to nearly zero with the detectors exposed to the full-energy protons. After all delays have been set, the detector system is moved to an angle of 20° or 30° and quadrupoles Q15 and Q16 are reset to the initial power settings. A target is placed in position and the proton beam is increased to give a (12345) count rate of approximately 50 counts per second. The inputs to all coincidence units are again checked to make certain that the system is functioning properly with both low- and high-energy particles incident on the detectors.

Analyzer System

The (TPHC) and (E_5) analog signals from the electronic system were digitized by two fast ADC's (100-MHz clock rate) and stored in a 128 by 128 channel array. After each test the data stored in the memory were transferred to seven-track computer compatible tape for off-line data analysis.

SYSTEM PERFORMANCE

Time Calibration

The time calibration of the spectrometer system was performed at $\phi = 0°$, that is, the detectors were in the direct beam. A low count rate of approximately 50 counts per second was used to minimize count-rate distortions in the time spectra. After accumulating greater than 20 000 counts in the time spectrum, a delay of 32 nsec was inserted in the stop input to the TPHC, and then a second time spectrum was produced. In figure 6 the time-of-flight (TOF) spectrum of the direct prompt proton beam is shown with a least squares fitted Gaussian curve. The time per analyzer channel was obtained by dividing the 32-nsec time delay by the difference between centroids of the direct and delayed time spectra. For the spectrum shown the time per channel is 0.29 nsec, and the time corresponding to the full width at half maximum (FWHM) is $\Delta t_f = 0.39$ nsec. The small peak in the spectrum was observed in all calibration spectra and was assumed to be pi-mesons from the last leg of the beam transport system.

The position of the direct-beam time spectrum and its width were checked at least once a day unless there was a power failure or malfunction in the electronic apparatus. The data on which this report is based were taken over a period of 3 days, and five time calibration checks were made. During this period the centroids of the time spectra maintained an average TOF channel number of 115.90 ± 0.23 and an average FWHM of 1.26 ± 0.05 channels.

The time of flight of a particle of known mass between two fixed points is given by the relativistic expression

$$t_f = \frac{d}{c} \frac{K + mc^2}{\sqrt{\left(K + mc^2\right)^2 - m^2c^4}} \tag{1}$$

where

d	distance of flight, m
c	speed of light, 2.99793×10^8 m/sec
K	kinetic energy of particle, MeV

m rest mass, kg

t_f time of flight over distance d, sec

By solving for kinetic energy K in equation (1), the kinetic energy of a particle of mass m with flight time t_f can be calculated from

$$K = mc^2\left[\frac{1}{\sqrt{1 - \left(\frac{d}{t_f c}\right)^2}} - 1\right] \tag{2}$$

The flight time t_f of the direct proton beam ($K = 558 \pm 7$ MeV (ref. 11), $m = 1.67 \times 10^{-27}$ kg) over the 4.88-m flight path d is calculated from equation (1) to be 20.89 ± 0.06 nsec. The energy spread in the incident proton beam therefore corresponds to a time spread Δt_{beam} of 0.12 nsec. Thus, the instrumental time resolution of the system (FWHM) is given by

$$\Delta t_{sys} = \sqrt{(\Delta t_f)^2 - (\Delta t_{beam})^2} = 0.37 \text{ nsec}$$

The intrinsic time resolution of the TPHC was found to be less than 15 psec (FWHM) and therefore makes a negligible contribution to the system time resolution.

Substituting into equation (2) the time variation of ±0.06 nsec in the centroid of the direct-beam time spectrum over the period of these measurements results in an energy variation of ±7 MeV at 558 MeV. The energy resolution $\Delta K/K$ of the time-of-flight system is obtained by differentiating equation (2) and substituting equation (1) for t_f:

$$\frac{\Delta K}{K} = \left(\frac{c}{d}\right)\left(\frac{K}{mc^2}\right)^2\left(1 + \frac{2mc^2}{K}\right)^{3/2} \Delta t_f \tag{3}$$

In figure 7 the energy resolution of the system is plotted as a function of particle kinetic energy for protons, deuterons, and tritons with energies from 50 to 600 MeV.

Resolution of Large Scintillator

The large (12.7 cm in diameter and 30.48 cm long) plastic scintillator used in energy detector 5 could stop approximately 220-MeV protons and 300-MeV deuterons. For particles of greater energy, detector 5 acted as a thick dE/dx counter. (The notation dE/dx denotes the rate of energy loss per unit pathlength in scintillator.) The raw response of this detector to 56 ± 0.8 MeV protons, 112 ± 1.6 MeV deuterons, and 168 ± 2.4 MeV tritons is shown in figure 8(a). The proton-deuteron separation is approximately 25 energy channels, whereas the deuteron-triton separation is about 22 channels. The proton and deuteron data give an energy per channel of 2.24 MeV. The FWHM for the proton and deuteron peaks is approximately 4.5 MeV and 6.7 MeV, respectively.

In figure 8(b) the raw spectra for 100 ± 1.9 MeV protons and 200 ± 3.9 MeV deuterons are shown. Separation between peaks is about 42 energy channels which gives an energy resolution of 2.38 MeV/channel. The asymmetry of the proton peak may be due to energy losses through proton-neutron collisions and gamma-ray losses from excitation of the 4.4-MeV level in carbon. The asymmetry of the deuteron peak may be due to particle breakup with escape of the neutron and excitation of the nuclear levels in carbon.

The spectrum in figure 8(c) is from 200 ± 5.9 MeV protons stopping in the large scintillator. This spectrum and those in figures 8(a) and 8(b) were taken from the same two-dimensional spectrum of energy as a function of time of flight. At 200 ± 5.9 MeV the protons are within a few centimeters of penetrating the detector, and some shift in the peak position due to nonuniform light collection of the photomultiplier tube would be expected. Also, a larger percentage of the incident protons would be expected to undergo inelastic nuclear collisions and give rise to a larger low-energy tail. The energy resolution is approximately 19 MeV (FWHM) or roughly 10 percent for 200 ± 5.9 MeV protons.

The shape of the curves for protons with energies greater than 200 MeV changes rapidly with increasing energy. Figure 8(d) shows the output from detector 5 for 558-MeV incident protons. Note that the low-energy tail is nearly absent, but a high-energy tail now appears. This curve has not been examined in depth; it is thought that the high-energy tail is due to cascade reactions in the scintillator. The most probable energy is approximately 100 MeV, and the peak has a Gaussian shape down to about 1/20 height. The computed energy loss by 558-MeV protons in 30.48 cm of plastic scintillator is 85 MeV.

Count-Rate Linearity of Logic System

The logic setup of the electronics system requires that a particle pass through all five detectors and initiate coincidence signals (12) and (345) within a time period of less than 50 nsec. The logic modules used for the (12) and (345) coincidences were operated with a pulse-pair resolution of 5 and 15 nsec, respectively, but the pulse-pair resolution for the (12345) coincidence was approximately 55 nsec. The linear signal processing modules could only operate at less than 30-μsec pulse-pair resolution; therefore such units as the linear gate and stretcher module for detector 5 and the TPHC limited the system's count rate and linearity. Because the gate unit output represents the highest coincidence requirement of the system, that is, the (12345 + E_5 + TPHC) coincidence, it has the worst pulse-pair resolution of the electronics system and the most sensitivity to count rate. The percent dead time t_d of the logic system is therefore defined as

$$t_d = \left(1 - \frac{N_{gate}}{N_{12345}}\right) \times 100$$

where N_{gate} is the number of gate counts and N_{12345} is the number of (12345) coincidence counts.

Tests on the count-rate linearity of the electronics system as a function of beam intensity were made at angles of 10° and 20° on targets of aluminum (0.635 cm thick) and lead (1.27 cm thick). The coincidence counts from the (12), (345), and (12345) logic modules, as well as the counts from the TPHC and gate units, were integrated along with the ion-chamber current over a preset time interval. The integrated count from each unit was divided by the ion-chamber integrated current, and these ratios are plotted as a function of integrated ion-chamber current in figure 9. The solid lines in each figure are a visual guide. The proton beam intensity was varied by a factor of 200 from the maximum cyclotron output to a minimum current which produced less than 0.1 count per second in the (12345) coincidence unit. For each data point shown the beam current was constant over the integration period.

The data at 10° (fig. 9(a)) show a system dead time of less than 5 percent for currents near 1.39×10^{-11} ampere (10^{-9} coulomb for an integration time of 72 sec). At 1.39×10^{-10} ampere (10^{-8} coulomb), the dead time is 14 percent and then rapidly increases to 60 percent as the beam intensity increases by an additional factor of 10. Above 1.39×10^{-9} ampere (10^{-7} coulomb), the TPHC unit, and consequently the gate unit, appears to saturate. The ratios for (345) and (12345) coincidence counts show an approximate 4-percent increase of the range of integrated current. The ratio for the (12) coincidence count shows a strong nonlinear increase with increasing current; this behavior was not investigated.

At 20° (fig. 9(b)) the ratios for (12) and (345) coincidence counts show a slight change of approximately 1 percent, but the ratio for the (12345) count is constant over the entire current range. The dead time of the system at 20° for a current of 1.67×10^{-11} ampere (10^{-9} coulomb for an integration time of 60 sec) is approximately 2 percent. The dead time slowly increases to 16 percent at 1.67×10^{-9} ampere (10^{-7} coulomb) and then rapidly increases to 30 percent at the highest current.

For all tests at 20° and at greater angles, the beam current was set to produce a steady ion-chamber current between 10^{-10} and 6×10^{-10} ampere. At 10° the currents used were generally 10^{-10} to 2×10^{-10} ampere. Thus, the system dead time for all measurements was approximately 5 percent.

Detection Efficiency of Detectors 1 to 4 and Time Resolution

In the design of this time-of-flight detection system a compromise had to be reached between the scintillator thickness of detectors 1, 2, 3, and 4 (see fig. 1), the desired time resolution, and the degree of multiple scattering in detectors 1 and 2 that could be tolerated. Because the time resolution of a detector (scintillator and photomultiplier tube) is proportional to the square root of the average number of photoelectrons released per detected event, it is desirable to have a thick scintillator of high light output per unit energy deposited and a photomultiplier tube of high gain, fast rise time, small transit time spread, and high quantum efficiency to convert the scintillator light into photoelectrons. All the above scintillator and photomultiplier tube characteristics determine the amplitude and shape of the output pulse signal.

Generally, the output signal is fed to a discriminator circuit which has a fixed threshold. Ideally, the average amplitude of the pulse from particles of the same energy passing through a detector should be much greater than the threshold to ensure that events are not lost through random fluctuations in the amplitude. However, the thicker the detectors, the greater the number of particles scattered out of the detection system. This outscattering has the effect of reducing the solid angle of the detection system and increasing the amount of cyclotron running time to accumulate a secondary particle spectrum.

Through a process of trial and error in using scintillators of various thicknesses and different mounting configurations, the dimensions in table I for detectors 1 to 4 were used to accumulate data. The combined thickness of detectors 1 and 2 produced a calculated decrease by a factor of 3 in the system solid angle for 40-MeV protons, but a negligible decrease for 600-MeV protons. Since detectors 2 and 4 are used for timing, they have the thicker scintillators. As shown in figure 5 the signals from detectors 1 and 3 were fed directly to pulse discriminator units, whereas the signals from detectors 2 and

4 were split into two half-amplitude signals which were each fed to a discriminator and to a CFTD. The threshold levels on these six discriminators were set slightly above the random dark current noise pulses from the photomultiplier tubes. With no beam and no light leaks around the scintillators, the count rate from the discriminators was generally less than 100 counts per second.

A fast-rise-time oscilloscope was used to observe the shape and amplitude of the output signals from detectors. The signals produced from Co^{60} gamma rays absorbed by the detectors had peak amplitudes of 3 to 4 V, and a clean, nearly Gaussian shape. When exposed to a direct beam of 558-MeV protons which produced approximately 50 counts per second, all detectors produced a narrow, nearly Gaussian trace. The pulse amplitude from detector 4 was approximately 6 V, whereas the output from detector 1 was approximately 3.5 V. Since the threshold levels on the discriminators were set at 100 mV or less, the input signals were at least a factor of 30 above the threshold, and thus nearly 100-percent detection efficiency was ensured.

The CFTD's used in this experiment had a 20:1 dynamic range but required input signals from 50 mV to 1 V. Since the energy loss rate of protons in the plastic scintillator varies by a factor of 5.88 from 40 MeV to 558 MeV, the input signals to the two CFTD's were attenuated to a level of 160 mV for 558-MeV protons incident on the detectors.

As shown in figure 5 the output signals from the two CFTD's are fed to the TPHC, and the (345) coincidence signal gates on the TPHC. Under ideal conditions the count rate in the TPHC should equal the (12345) coincidence rate if events are not lost because of improper setting of the thresholds on the CFTD's. In practice, however, the 4-μsec pulse-pair resolution of the TPHC precludes any significant test to determine discrepancies. It is observed, however, from measurements of dead time, that the count rates for the TPHC and (12345) coincidence are the same up to an average rate of approximately 30 counts per second for data taken at the 20° scatter angle. For an average rate of 60 counts per second, the ratio of TPHC counts to (12345) counts is 0.94, whereas for a rate of 460 counts per second, the ratio drops to 0.78. The low equal count rate indicates that the threshold levels on the CFTD's are properly set. The decrease in this ratio at higher count rates is indication of the large dead time of the TPHC.

Background Levels

In the original design of this detection system it was assumed that all detectors would have to be shielded from particles scattered from the end of the beam transport system as well as from neutral radiation produced in the beam dump area. For the first test of the detection system, considerable physical effort was expended in shielding the detectors with lead bricks. Although the shielding produced a sharp decrease in the background count rate in the detectors, it was apparent that the source of the background radiation was the poorly defined incident proton beam. After obtaining an incident beam of very small divergence, the coincidence count rates in the detectors sets were low enough to eliminate the need for shielding.

As examples of the foreground and background levels in the data, figure 10 shows integrated count per channel as a function of TOF channel number for data taken at angles of 10°, 20°, 40°, and 60° and the background levels at the same angles. For each pair of curves, all conditions are the same except that the target was removed to make the background measurements. As expected, the highest background levels occur at the smaller angles. The shapes of the background curves are not constant but vary with angle; however, they have the same general shape as the data curves. The ratio of the integrated background spectrum to the integrated data spectrum is 0.0143, 0.0115, 0.0029, and 0.0032 for angles of 10°, 20°, 40°, and 60°, respectively. The highest ratio is found in the 10° data of figure 10(a), where the ratio varies around 0.01 but occasionally reaches 0.03 in the vicinity of the quasi-elastic peak. The background to foreground ratio for any given channel in figure 10(b) for the 20° data does not exceed 0.024. For the 40° data (fig. 10(c)) the ratio is less than 0.01, and for the 60° data (fig. 10(d)) the ratio is less than 0.005.

DATA CORRECTIONS AND ERROR ASSIGNMENT

Multiple Scattering Correction to Detection System Solid Angle

Because secondary particles do not originate at a single point in the target, an average or weighted solid angle must be determined not only as a function of the incident beam intensity over the target but also as a function of multiple scattering in the first set of detectors.

If the target is considered a point source, the solid angle Ω_4 subtended by detector 4 is given approximately by

$$\Omega_4 = \frac{A_4}{R_4^2} = \frac{S_4^2}{R_4^2} .$$

where

A_4	surface area of detector 4, cm^2
R_4	distance from target to detector 4, 595 cm
S_4	length of side of detector 4, 4.30 cm

The weighted solid angle is defined by

$$\bar{\Omega}_4 \equiv W\Omega_4 \tag{4}$$

where W is a weighting factor which depends on the intensity distribution of secondary particles from the target and is a function of secondary particle type and energy K, thickness of detector set 1, and orientation of the target. It is assumed that a Gaussian distribution can adequately describe the multiple scattering from the 0.648 g/cm^2 thick scintillator material in the first set of detectors; that is, the probability P (per unit area) of finding a scattered particle a distance s from its unscattered position is given by (ref. 12)

$$P = \frac{1}{\sqrt{\pi r_o^2}} \exp\left(\frac{-s^2}{r_o^2}\right)$$

where

$$r_o = \frac{E_s}{\beta cp} \frac{\sqrt{x}\, l}{\sqrt{X_o}}$$

and where

x	thickness of detector set 1, cm
l	distance from detector 2 in plane containing detector 4

βc	velocity of particle
p	momentum of particle
E_s	$= 21$ MeV
X_o	radiation length, cm

A Monte Carlo computer program was developed to calculate the weighting factor W for the detector system shown in figure 1. For any given intensity distribution on the target, the program determines the number N of particles that intercept both detector sets 1 and 2 for no multiple scattering from detector set 1, and also the number N' of particles intercepting both detector sets with multiple scattering in detector set 1. For a given particle type, energy K, and angle ϕ of emission, the weighting factor is given by

$$W(\text{Type},K,\phi) = \frac{N'}{N}$$

Within statistical fluctuations the weighting factors are less than unity for proton energies used in the present experiment. Thus, the multiple scattering from the first detector set has the effect of reducing the solid angle of the detection system.

With an intensity distribution on the target, a particle type, a secondary energy K, and an angle ϕ given, a sufficient number of histories were run to reduce the statistical uncertainty in the weighting factor W to less than ±3 percent. The weighting factors used in the data analysis are shown in figure 11 as a function of energy. The error bars indicate the statistical uncertainty at selected energies.

Correction for the Energy Loss in Target and TOF System

If a particle with rest mass energy M and kinetic energy K is produced in the target and detected by the TOF system, the kinetic energy K' calculated from the measured time of flight t_f over a distance d between detectors 2 and 4 is given by

$$K' = mc^2\left[\frac{1}{\sqrt{1 - \left(\frac{d}{t_f c}\right)^2}} - 1\right] \tag{5}$$

where c is the speed of light in vacuo. The difference ΔK between K and K' represents the sum of energy lost in the target ΔK_t, in the air between the target and the first set of detectors ΔK_A, in the aluminum foil used for the enclosure windows and scintillator covers ΔK_{Al}, in the plastic scintillators 1 and 2 ΔK_s, and in the helium-filled gas bag between the two detector sets ΔK_{He}. Thus,

$$K - K' = \Delta K = \Delta K_t + \Delta K_A + \Delta K_{Al} + \Delta K_{He} + \Delta K_s$$

Since the rate of energy loss by a particle varies approximately as the inverse square of the particle's energy, ΔK for a 600-MeV proton passing through the system is much less than ΔK for a 50-MeV proton. If the energy loss in the target is ignored, the lowest energy for protons that can be observed by time of flight in this system was calculated to be approximately 47 MeV; that is, a proton with energy of 47 MeV from the target has just enough energy to pass through the system in the time interval set by the TPHC to satisfy the (12345) coincidence requirement. For a 47-MeV proton the energy lost in the system was calculated to be approximately 7 MeV, that is,

$$\Delta K_A + \Delta K_{Al} + \Delta K_s + \Delta K_{He} \approx 7 \text{ MeV}$$

The time range on the TPHC sets a 40-MeV energy cutoff for protons and a 80-MeV cutoff for deuterons. Therefore, a 47-MeV proton from the target possesses the minimum energy detectable by the time-of-flight measurement. To correct the observed spectra for this energy loss in the detection system, a method must be found to shift the energy scale in the increasing direction in a way consistent with the energy width of each channel which varies as a function of energy. It is also desirable to correct the energy scale for the energy lost in the target.

To calculate the energy loss in the target, a parallel beam of incident protons with radius r and a uniform cross-sectional intensity is assumed. The target has thickness τ and is normal to the incident particles. The axis of the TOF detection system intersects the beam center line at the center of the target, and ϕ is the angle between the beam line and the TOF axis. It is assumed that production of secondary particles is uniform throughout the volume defined by the incident beam diameter and the target thickness and that the secondary particles suffer no inelastic collisions in the target. The active volume of the target defined as that volume where interactions occur is a right circular cylinder of length τ and radius r. The projected cross-sectional area A of this volume viewed along the TOF axis (fig. 12(a)) is given by

$$A = \pi r^2 \cos \phi + 2r\tau \sin \phi$$

where the height is a constant, 2r, and the width of the area w varies with ϕ, that is,

$$w = \tau \sin \phi + 2r \cos \phi$$

The energy lost in the target ΔK_t by a particle of initial energy K_o is a function of target material, initial energy, and distance the particle travels through the target. In figure 12(b) the active volume is viewed perpendicular to the plane containing the beam center line and the TOF system center line. A set of rectangular coordinates with origin at the intersection of the beam center line and TOF center line at the center of the target is defined with the positive z-direction along the incident beam direction and the positive y-direction perpendicular to beam and TOF system center lines. The point P_o is the origin of a secondary particle leaving the target, and P_s is the point at which the particle leaves the target. It is assumed that the particle travels parallel to the TOF axis so that

$$y_o = y_s = \text{Constant}$$

The distance S_t traveled through the target is given by

$$S_t = \frac{\frac{\tau}{2} - z_o}{\cos \phi} \qquad \left(-\frac{\tau}{2} \leqq z_o \leqq \frac{\tau}{2}\right) \tag{6}$$

and the energy lost in the target ΔK_t is obtained by integrating the rate of energy loss $(dK/d\ell)_t$ in the target over the distance S_t,

$$\Delta K_t = \int_0^{S_t} \left(\frac{dK}{d\ell}\right)_t d\ell \tag{7}$$

where $d\ell$ is an element of length along the path S_t. The energy of the particle leaving the target K_t is given by

$$K_t = K_o - \Delta K_t$$

The energy lost in the TOF system is given by the following set of equations:

$$\Delta K_A = \int_0^{S_A} \left(\frac{dK}{d\ell}\right)_A d\ell \qquad \left(K_A = K_t\right) \tag{8}$$

$$\Delta K_{Al} = \int_0^{S_{Al}} \left(\frac{dK}{d\ell}\right)_{Al} d\ell \qquad \left(K_{Al} = K_A - \Delta K_A\right) \tag{9}$$

$$\Delta K_s = \int_0^{S_s} \left(\frac{dK}{d\ell}\right)_s d\ell \qquad \left(K_s = K_{Al} - \Delta K_{Al}\right) \tag{10}$$

$$\Delta K_{He} = \int_0^{S_{He}} \left(\frac{dK}{d\ell}\right)_{He} d\ell \qquad \left(K_{He} = K_s - \Delta K_s\right) \tag{11}$$

where the subscripts A, Al, s, and He denote the absorbing material in the TOF system – air, aluminum, scintillator, and helium, respectively; and where K_A, K_{Al}, K_s, and K_{He} are the kinetic energies of the particle entering the respective absorbing material. The energy measured by the time-of-flight technique is given by

$$K = K_o - \left(\Delta K_t + \Delta K_A + \Delta K_{Al} + \Delta K_s + \Delta K_{He}\right) \tag{12}$$

Because of the random production of secondary particles in the active volume of the target, a Monte Carlo computer program was written to simulate the transport of secondary particles through the target and TOF system. For each computer event at a given angle ϕ, a random point $P_o(x_o,y_o,z_o)$ is chosen within the active target volume and an initial energy K_o is chosen at random between 47 MeV and 600 MeV for protons. Equations (7) to (11) are evaluated sequentially and K is obtained from equation (12). A TOF channel number is then computed for K and K_o. This process is repeated for a large number of events, and then for each TOF channel, the ratio of the number of events corresponding to energy K_o is divided by the number of events of energy K that fall in that channel. This ratio is then used as a multiplicative factor to correct the observed spectra for energy loss in the target and TOF system.

In the data analysis this energy loss factor was combined with the multiple scattering weighting factor W to provide a single multiplicative factor as a function of particle type, particle energy, and angle of deflection. In figure 13 the energy distribution of the combined multiplicative factor for protons and deuterons is shown for a 2.35 g/cm^2 thick beryllium target for an angle of scatter of 20°. These curves are typical of the raw data correction factors used for other target materials. The width of each curve represents the statistical uncertainty in the calculations.

Error Assignment to Cross-Section Values

A summary of the systematic and statistical errors associated with the cross-section values obtained by the TOF system is presented in this section. Three sources of error which have not been discussed in this report are uncertainty in the total number of incident protons, variations in target thickness, and target purity. In reference 13 the details of calibrating ion chambers with the SREL Faraday cup are given. The estimated error associated with the cup is shown to be less than 1 percent and the uncertainty in the accuracy of the current integration and current source calibration is taken as ±2 percent. The uncertainty in the mean energy to produce an ion pair in helium is taken as ±3 percent. Thus, the error in measuring the incident number of protons is

$$\left(0.01^2 + 0.02^2 + 0.03^2\right)^{1/2} \approx 0.04$$

The thickness of all targets was measured to ±0.01 mm and in no case did the variations in thickness exceed ±1 percent. All targets used in this report were commercially available and were at least 98 percent pure. No corrections were made to the data for trace contaminants.

The uncertainty in the time measurements is taken as 0.39 nsec. Since the energy is a nonlinear function of time, the error in the energy calculation must be obtained from equation (3). The error varies from ±1.6 percent at 50 MeV to ±7.75 percent at 558 MeV for protons. The energy resolution for deuterons and tritons is also calculated from equation (3).

The uncertainty in the energy-scale correction due to energy loss in the target and TOF system is a function of absorber mass and thickness. For a 1.27-cm-thick beryllium target and a scattering angle of 20°, the uncertainty varies from ±3.75 to ±5.5 percent for protons. The accuracy of the energy loss rates used in the computer experiment was given as ±1 percent (ref. 14), and the accuracy of the energy loss calculation is taken as ±2 percent. The statistical error of the experiment varied with energy and particle type from ±3 to ±5 percent. No correction was made to the energy scale above 300 MeV for either protons or deuterons, since the energy resolution of the system is then larger than any shift due to energy loss in the target and detection system.

The uncertainty in the solid-angle calculation for the detection system is assigned a value of ±5 percent, assuming that the Gaussian distribution approximation to multiple scattering of charged particles is good to ±4 percent and that the statistical errors in the computations are less than ±3 percent.

The detection efficiency of the TOF detectors is assumed to be greater than 98 percent, and the dead-time loss in the (12345) coincidence count is less than 1 percent at the counting rates used in this experiment.

If the statistical error of the raw data is ignored, the error of the double differential cross sections for protons varies from ±9.3 percent at 50 MeV to ±11.4 percent at 558 MeV. For deuterons the errors are approximately ±8 percent at 90 MeV and approximately ±8.3 percent at 350 MeV. The statistical error assigned to the raw data is the square root of the number of counts in a given channel. The uncertainty in the cross sections given in this report does include the statistical variations of the raw data.

RESULTS

As stated previously the two-parameter analyzer system converts the analog signals from detector 5 and the TPHC to a channel number from 1 to 128. At the end of each test the analyzer memory content was transferred to magnetic tape for off-line computer analysis. The raw data obtained from a 2.35 g/cm^2 thick beryllium target under 558-MeV irradiation at an angle of 20° are shown in figure 14 as a computer-drawn contour plot.

The upper, thinly populated line of symbols denotes the secondary deuteron spectrum. The break or foldover of this curve occurs when the deuterons penetrate large detector 5 and begin losing less than their total kinetic energy. Note that the deuteron spectrum crosses the proton spectrum and appears to terminate around TOF channel number 96 and energy channel number 62. The heavy band of symbols indicates the proton spectrum. The foldover is again due to the particles penetrating detector 5, and the distribution of symbols around TOF channel 113 represents the quasi-elastic scatter peak. The grouping of symbols from TOF channels 120 to 128 indicates pi-meson production through proton-proton interactions in the target.

The two dashed lines in figure 14 represent the calculated shapes of the proton and deuteron distributions, and the solid lines connect the peak values of the energy channel pulse-height distributions for each TOF channel number. The agreement between the experimental and calculated shapes is quite good except for high-energy protons for which the calculated curve begins to diverge from the experimental data.

In figure 15 the raw data from a 2.35 g/cm^2 thick beryllium target at angles of 20° and 50° are shown as computer-drawn isometric projections to indicate the quality of the raw data and to show the change in the spectra from an angle of scatter of 20° to 50°. In these two plots all channels with one or more events per channel are used for the display.

In figure 16 the analyzed data are plotted as differential cross sections (mb/sr-MeV) as a function of secondary particle energy in MeV. (Tabulated cross sections are found in table II.) The quasi-elastic proton peak attains its maximum value at 476 ± 26 MeV which agrees closely with 474 MeV computed for proton-proton elastic scattering at 558 MeV at 20°. The deuteron spectra were terminated at TOF channel 88 which corresponds to a deuteron energy of 368 MeV. As can be seen in figure 14 the deuteron spectrum does continue up to TOF channel 96 which means that deuterons are produced with energies of 468 ± 15 MeV. The energy of a recoil deuteron in an elastic collision with a 558-MeV proton is 444 MeV at an angle of 20°. It therefore appears that deuterons exist as a bound system in the beryllium nucleus and that they do elastically scatter when bombarded by 558-MeV protons.

No attempt has been made to analyze the pi-mesons that appear in the secondary particle spectra other than to note what appears to be a peak at TOF channel 126 (fig. 14) which would represent a pi-meson energy of approximately 340 MeV. From the relativistic kinematics of proton-proton interactions at 558 MeV, the energy of a pi-meson emitted at 20° in the laboratory system is approximately 348 MeV. Another general feature of the proton and deuteron spectra is that the number of deuterons is approximately 10 percent of the number of protons at the same energy below the quasi-elastic peak.

An effort was made to compare the cross sections obtained by the TOF spectrometer system with values obtained by a momentum analyzing system. The only available data found on proton-beryllium interactions near the SREL cyclotron energy were those of L. S. Azhgirey et. al. (ref. 15) who give the cross sections for the production of secondary protons at 18° from beryllium under 660-MeV-proton bombardment. They found a maximum value of 0.75 mb/sr-MeV for the quasi-elastic peak which agrees well with the 0.75 ± 0.07 mb/sr-MeV obtained using the TOF system with incident 558-MeV protons.

SUMMARY OF RESULTS

A time-of-flight and energy spectrometer system has been constructed and used to obtain the double differential scattering cross sections for protons, deuterons, and tritons from materials under 558-MeV-proton irradiation. The 0.39-nsec time resolution of the system gave an energy resolution for the 488-cm flight path of ±1.6 percent at 50 MeV and ±7.75 percent at 558 MeV for protons. The 12.7-cm-diameter by 30.48-cm-long energy detector had a resolution of 4.5 MeV at full width at half maximum for approximately 56-MeV protons and 19 MeV full width at half maximum for 200-MeV protons. This two-parameter system was able to clearly separate deuterons from protons up to approximately 368 MeV for deuterons.

Corrections to the raw data were required to account for the effective decrease in detection solid angle caused by the outscattering of particles from the first set of detectors in the system. A second correction was required to adjust the raw data energy scale for energy lost by the secondary particles in the target and in the detection system.

The systematic error assignment varied from 9.3 percent at 50 MeV to 11.4 percent at 558 MeV for protons. This error assignment includes uncertainties in the solid angle, in the energy-scale corrections, and in the incident proton beam calculations. It also includes uncertainties in target thickness, detection efficiency, and dead-time estimates.

The double differential cross sections (mb/sr-MeV) for protons produced at an angle of 20° from a 2.35 g/cm^2 thick beryllium target under 558-MeV-proton irradiation were compared with similar data obtained with a momentum analyzing system using 660-MeV incident protons. The maximum value of 0.75 ± 0.07 mb/sr-MeV, obtained for the quasi-elastic peak using the scintillation spectrometer system, agrees well with the reported value of 0.75 mb/sr-MeV, obtained with the momentum analyzing system.

Langley Research Center
National Aeronautics and Space Administration
Hampton, Va. 23665
June 5, 1975

REFERENCES

1. Siegel, R. T.: High Energy Neutron Detectors. Encyclopedia of Physics, Volume XLV, Springer-Verlag, 1958, pp. 487-517.
2. Peelle, R. W.; Love, T. A.; Hill, N. W.; and Santoro, R. T.: Differential Cross Sections for the Production of Protons in the Reactions of 160-MeV Protons on Complex Nuclei. ORNL-3887, U.S. At. Energy Comm., Sept. 1966.
3. Bertrand, F. E.; Burras, W. R.; Hill, N. W.; Love, T. A.; and Peelle, R. W.: A High Resolution Spectrometer System With Particle Identification for 1 Through 60 MeV Hydrogen and Helium Particles. Nucl. Instrum. & Methods, vol. 101, no. 3, June 15, 1972, pp. 475-492.
4. Turkot, F.; Collins, G. B.; and Fujii, T.: Deuteron Production in p-p Collisions in the Range 1.5 to 2.5 BeV. Phys. Rev. Lett., vol. 11, no. 10, Nov. 15, 1963, pp. 474-476.
5. Fitch, V. L.; Meyer, S. L.; and Piroué, P. A.: Particle Production at Large Angles by 30- and 33-Bev Protons Incident on Aluminum and Beryllium. Phys. Rev., second ser., vol. 126, no. 5, June 1, 1962, pp. 1849-1851.
6. Schwarzschild, A.; and Zupančič, Č.: Production of Tritons, Deuterons, Nucleons, and Mesons by 30-GeV Protons on A1, Be, and Fe Targets. Phys. Rev., second ser., vol. 129, no. 2, Jan. 15, 1963, pp. 854-862.
7. Melissinos, A. C.; Yamanouchi, T.; Fazio, G. G.; Lindenbaum, S. J.; and Yuan, L. C. L.: π-Meson Production in 2.9-BeV p-p Collisions. Phys. Rev., second ser., vol. 128, no. 5, Dec. 1, 1962, pp. 2373-2381.
8. Edge, R. D.; and Knox, H. H.: Deuteron Production in Nuclei by Protons of From 1 to 3-BeV. Phys. Rev., second ser., vol. 184, no. 4, Aug. 20, 1969, pp. 1034-1040.
9. Costrell, Louis: Standard Nuclear Instrument Modules. TID-20893 (Rev. 3), At. Energy Comm., Dec. 1969.
10. Gedcke, D. A.; and McDonald, W. J.: Design of the Constant Fraction of Pulse Height Trigger for Optimum Time Resolution. Nucl. Instrum. & Methods, vol. 58, no. 2, Jan. 1968, pp. 253-260.
11. Beck, Sherwin M.; and Powell, Clemans A., Jr.: A Focused Čerenkov Radiation Detector for Proton Beam Energy Measurements. NASA TN D-6194, 1971.
12. Sternheimer, R. M.: Multiple Scattering Correction for Counter Experiments. Rev. Sci. Instrum., vol. 25, no. 11, Nov. 1954, pp. 1070-1075.

13. Beck, Sherwin M.: Design, Performance, and Calculated Error of a Faraday Cup for Absolute Beam Current Measurements of 660-MeV Protons. NASA TN D-7858, 1975.

14. Janni, Joseph F.: Calculations of Energy Loss, Range, Pathlength, Straggling, Multiple Scattering, and the Probability of Inelastic Nuclear Collisions for 0.1- to 1000-Mev Protons. AFWL-TR-65-150, U.S. Air Force, Sept. 1966. (Available from DDC as AD 643 837.)

15. Azhgirey, L. S.; Vzorov, I. K.; Zrelov, V. P.; Mescheryakov, M. G.; Neganov, B. S.; Ryndin, R. M.; and Shabudin, A. F.: Nuclear Interactions of 660 MeV Protons and the Momentum Distribution of Nucleons in Nuclei. Nucl. Phys., vol. 13, no. 2, Oct. 2, 1959, pp. 258-280.

TABLE I.- DIMENSIONS OF SCINTILLATORS AND THICKNESS OF ABSORBERS ALONG FLIGHT PATH

Component	Dimensions, cm	Thickness, g/cm^2
Scintillator 1[a]	4.55 by 4.30 by 0.158	0.162
Scintillator 2[a]	2.54 (diam) by 0.476	.486
Scintillator 3[a]	4.55 by 4.30 by 0.158	.162
Scintillator 4[a]	4.30 by 4.30 by 0.635	.648
Scintillator 5[a]	12.7 (diam) by 30.48	31.090
Helium[b]	487.68 (length of volume)	.089
Enclosure windows (4)[c]	0.00128 (thickness)	.007
Reflective covers on scintillators (9)[d]	0.00254 (thickness)	.062

[a] Density of scintillator, 1.02 g/cm^3.

[b] Density of helium, 0.1785 mg/cm^3.

[c] Density of polyethylene terephthalate, 1.380 to 1.395 g/cm^3.

[d] Density of aluminum, 2.702 g/cm^3.

TABLE II.- DOUBLE DIFFERENTIAL CROSS SECTIONS FOR PRODUCTION OF PROTONS AND DEUTERONS AT 20° FROM A 2.35 g/cm^2 THICK BERYLLIUM TARGET UNDER 558-MeV-PROTON IRRADIATION

(a) Secondary protons

Energy, MeV	Cross section, mb/sr-MeV	Energy, MeV	Cross section, mb/sr-MeV
60.7 ± .8	.241 ± .021	132.4 ± 3.0	.194 ± .016
61.6 ± .9	.240 ± .021	135.5 ± 3.1	.188 ± .015
62.5 ± .9	.232 ± .020	138.7 ± 3.2	.196 ± .016
63.5 ± .9	.194 ± .017	142.1 ± 3.3	.204 ± .017
64.5 ± .9	.189 ± .016	145.5 ± 3.5	.196 ± .016
65.4 ± 1.0	.213 ± .018	149.1 ± 3.6	.194 ± .016
66.5 ± 1.0	.181 ± .016	152.9 ± 3.8	.197 ± .016
67.5 ± 1.0	.204 ± .018	156.8 ± 3.9	.196 ± .016
68.6 ± 1.0	.223 ± .020	160.8 ± 4.1	.185 ± .015
69.7 ± 1.1	.229 ± .020	165.1 ± 4.3	.181 ± .015
70.8 ± 1.1	.187 ± .016	169.5 ± 4.5	.179 ± .015
71.9 ± 1.1	.265 ± .023	174.1 ± 4.7	.183 ± .015
73.1 ± 1.1	.250 ± .022	178.9 ± 4.9	.175 ± .015
74.3 ± 1.2	.246 ± .022	184.0 ± 5.1	.182 ± .015
75.5 ± 1.2	.239 ± .021	189.2 ± 5.4	.182 ± .016
76.8 ± 1.2	.241 ± .021	194.8 ± 5.6	.174 ± .015
78.1 ± 1.3	.205 ± .018	200.6 ± 5.9	.178 ± .016
79.4 ± 1.3	.222 ± .020	206.7 ± 6.2	.183 ± .016
80.8 ± 1.3	.202 ± .018	213.1 ± 6.5	.176 ± .015
82.2 ± 1.4	.235 ± .021	219.8 ± 6.9	.178 ± .016
83.7 ± 1.4	.242 ± .021	226.9 ± 7.2	.174 ± .015
85.2 ± 1.5	.226 ± .020	234.4 ± 7.6	.161 ± .014
86.7 ± 1.5	.226 ± .020	242.3 ± 8.1	.159 ± .014
88.3 ± 1.5	.229 ± .020	250.6 ± 8.6	.152 ± .013
89.9 ± 1.6	.222 ± .019	259.5 ± 9.1	.148 ± .013
91.6 ± 1.6	.225 ± .020	268.9 ± 9.6	.134 ± .012
93.3 ± 1.7	.224 ± .019	278.9 ± 10.3	.135 ± .012
95.0 ± 1.7	.206 ± .018	289.5 ± 10.9	.123 ± .011
96.9 ± 1.8	.195 ± .017	300.9 ± 11.7	.123 ± .011
98.7 ± 1.9	.215 ± .019	313.0 ± 12.5	.118 ± .010
100.7 ± 1.9	.226 ± .020	326.0 ± 13.4	.119 ± .011
102.7 ± 2.0	.202 ± .018	339.9 ± 14.4	.131 ± .012
104.7 ± 2.0	.205 ± .018	354.9 ± 15.5	.155 ± .014
106.8 ± 2.1	.210 ± .018	371.1 ± 16.8	.179 ± .016
109.0 ± 2.2	.209 ± .017	388.6 ± 18.2	.226 ± .021
111.3 ± 2.3	.206 ± .017	407.7 ± 19.8	.311 ± .029
113.6 ± 2.3	.225 ± .018	428.4 ± 21.6	.456 ± .043
116.1 ± 2.4	.205 ± .017	451.1 ± 23.7	.656 ± .062
118.6 ± 2.5	.204 ± .017	476.1 ± 26.2	.760 ± .073
121.1 ± 2.6	.206 ± .017	503.6 ± 29.0	.598 ± .058
123.8 ± 2.7	.198 ± .017	534.2 ± 32.3	.302 ± .030
126.6 ± 2.8	.203 ± .017	568.4 ± 36.2	.081 ± .008
129.5 ± 2.9	.195 ± .016	606.9 ± 40.9	.018 ± .001
		650.5 ± 46.6	.011 ± .001
		700.4 ± 53.6	.006 ± .000

TABLE II.- Concluded

(b) Secondary deuterons

Energy, MeV	Cross section, μb/sr-MeV	Energy, MeV	Cross section, μb/sr-MeV
108.4 ± 1.4	31.8 ± 5.2	222.6 ± 4.6	24.0 ± 2.6
109.9 ± 1.5	38.4 ± 5.8	227.3 ± 4.7	22.0 ± 2.4
111.4 ± 1.5	31.8 ± 5.1	232.1 ± 4.9	22.3 ± 2.4
113.0 ± 1.5	36.3 ± 5.4	237.1 ± 5.0	21.0 ± 2.3
114.6 ± 1.6	36.1 ± 5.4	242.3 ± 5.2	21.0 ± 2.3
116.3 ± 1.6	38.4 ± 5.5	247.6 ± 5.4	17.8 ± 2.0
118.0 ± 1.7	33.0 ± 4.9	253.2 ± 5.6	20.3 ± 2.2
119.7 ± 1.7	34.3 ± 5.0	258.9 ± 5.8	18.5 ± 2.0
121.5 ± 1.7	30.7 ± 4.6	264.9 ± 6.0	18.0 ± 1.9
123.3 ± 1.8	35.9 ± 5.0	271.1 ± 6.2	17.4 ± 1.9
125.1 ± 1.8	29.0 ± 4.3	277.5 ± 6.5	14.4 ± 1.6
127.0 ± 1.9	43.0 ± 5.6	284.1 ± 6.7	16.3 ± 1.7
128.9 ± 1.9	33.0 ± 4.6	291.0 ± 7.0	16.2 ± 1.7
130.9 ± 2.0	29.4 ± 4.2	298.2 ± 7.3	12.6 ± 1.4
132.9 ± 2.0	35.1 ± 4.7	305.7 ± 7.6	9.8 ± 1.1
135.0 ± 2.1	40.6 ± 5.2	313.5 ± 7.9	10.0 ± 1.1
137.1 ± 2.1	34.0 ± 4.5	321.6 ± 8.2	9.6 ± 1.1
139.3 ± 2.2	28.7 ± 3.9	330.1 ± 8.6	10.2 ± 1.1
141.6 ± 2.2	33.2 ± 4.3	338.9 ± 9.0	9.1 ± 1.0
143.9 ± 2.3	35.8 ± 4.5	348.2 ± 9.4	6.5 ± .8
146.2 ± 2.3	29.2 ± 3.9	357.8 ± 9.8	5.3 ± .6
148.6 ± 2.4	31.7 ± 4.1	367.9 ± 10.3	6.2 ± .7
151.1 ± 2.5	29.8 ± 3.8	378.4 ± 10.8	.0 ± .0
153.6 ± 2.5	28.9 ± 3.7	389.5 ± 11.3	.0 ± .0
156.2 ± 2.6	29.1 ± 3.7	401.1 ± 11.8	.0 ± .0
158.9 ± 2.7	30.7 ± 3.8	413.3 ± 12.4	.0 ± .0
161.6 ± 2.7	29.6 ± 3.7	426.1 ± 13.1	.0 ± .0
164.5 ± 2.8	37.2 ± 4.4	439.5 ± 13.8	.0 ± .0
167.4 ± 2.9	32.5 ± 3.9	453.7 ± 14.5	.0 ± .0
170.3 ± 3.0	30.5 ± 3.7	468.7 ± 15.3	.0 ± .0
173.4 ± 3.1	30.0 ± 3.6	484.5 ± 16.2	.0 ± .0
176.5 ± 3.1	34.2 ± 3.9	501.2 ± 17.2	.0 ± .0
179.8 ± 3.2	25.0 ± 3.1	518.9 ± 18.2	.0 ± .0
183.1 ± 3.3	25.4 ± 3.1	537.7 ± 19.3	.0 ± .0
186.5 ± 3.4	27.7 ± 3.2	557.7 ± 20.5	.0 ± .0
190.1 ± 3.5	27.4 ± 3.2	579.0 ± 21.9	.0 ± .0
193.7 ± 3.6	27.8 ± 3.2	601.6 ± 23.4	.0 ± .0
197.5 ± 3.8	26.1 ± 3.0	625.9 ± 25.0	.0 ± .0
201.3 ± 3.9	23.7 ± 2.7	651.8 ± 26.8	.0 ± .0
205.3 ± 4.0	24.0 ± 2.7	679.7 ± 28.9	.0 ± .0
209.4 ± 4.1	23.6 ± 2.7	709.7 ± 31.1	.0 ± .0
213.7 ± 4.3	24.3 ± 2.7	742.1 ± 33.6	.0 ± .0
218.1 ± 4.4	22.4 ± 2.5	777.1 ± 36.5	.0 ± .0

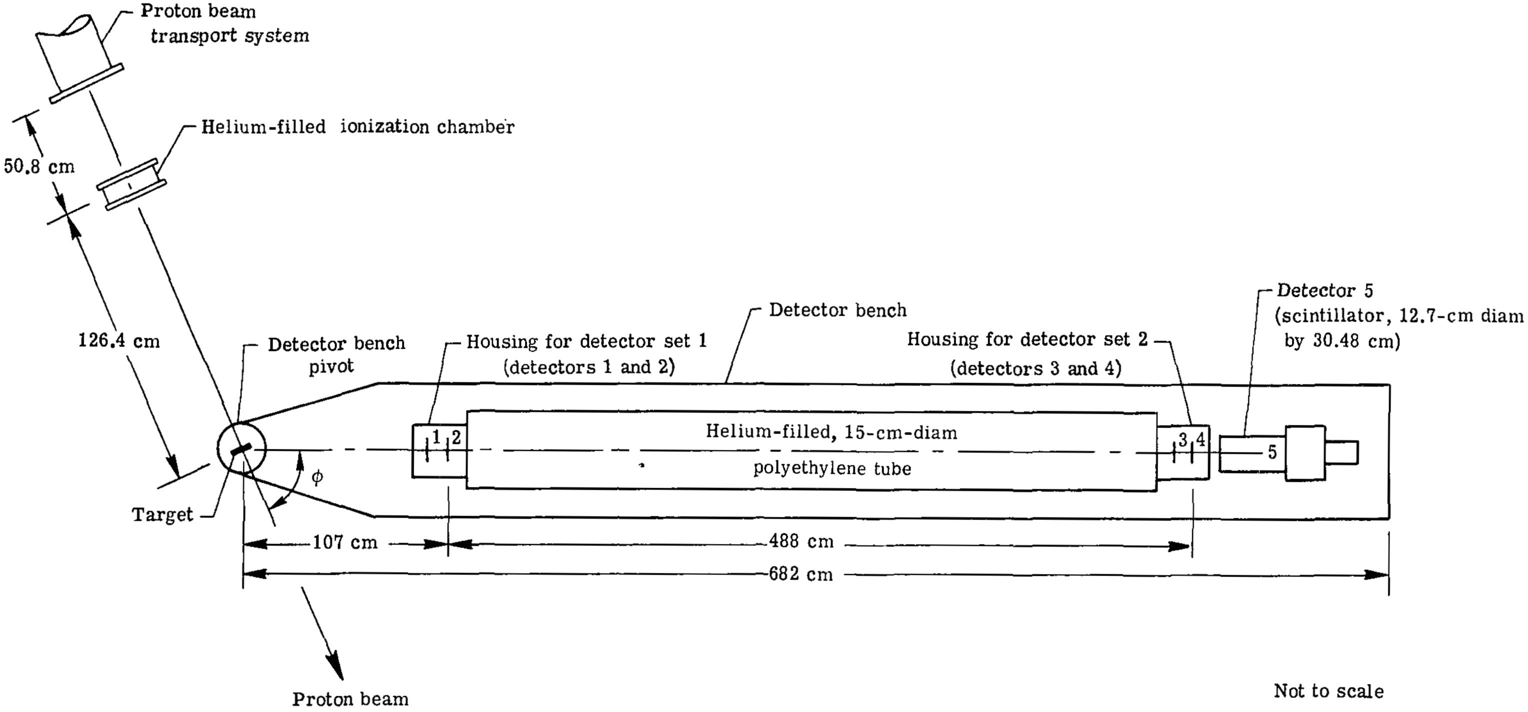

Figure 1.– Diagram of time-of-flight and energy spectrometer system.

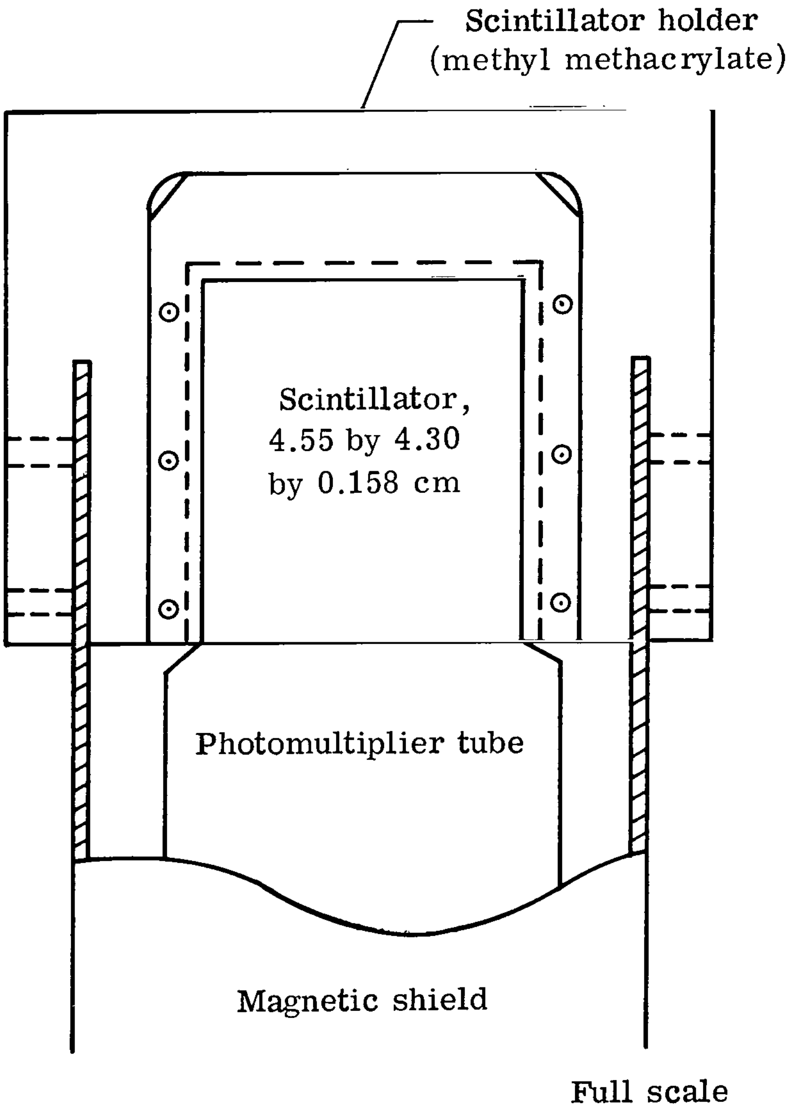

(a) Detectors 1 and 3.

Figure 2.– Mounting configurations for detectors 1 to 4.

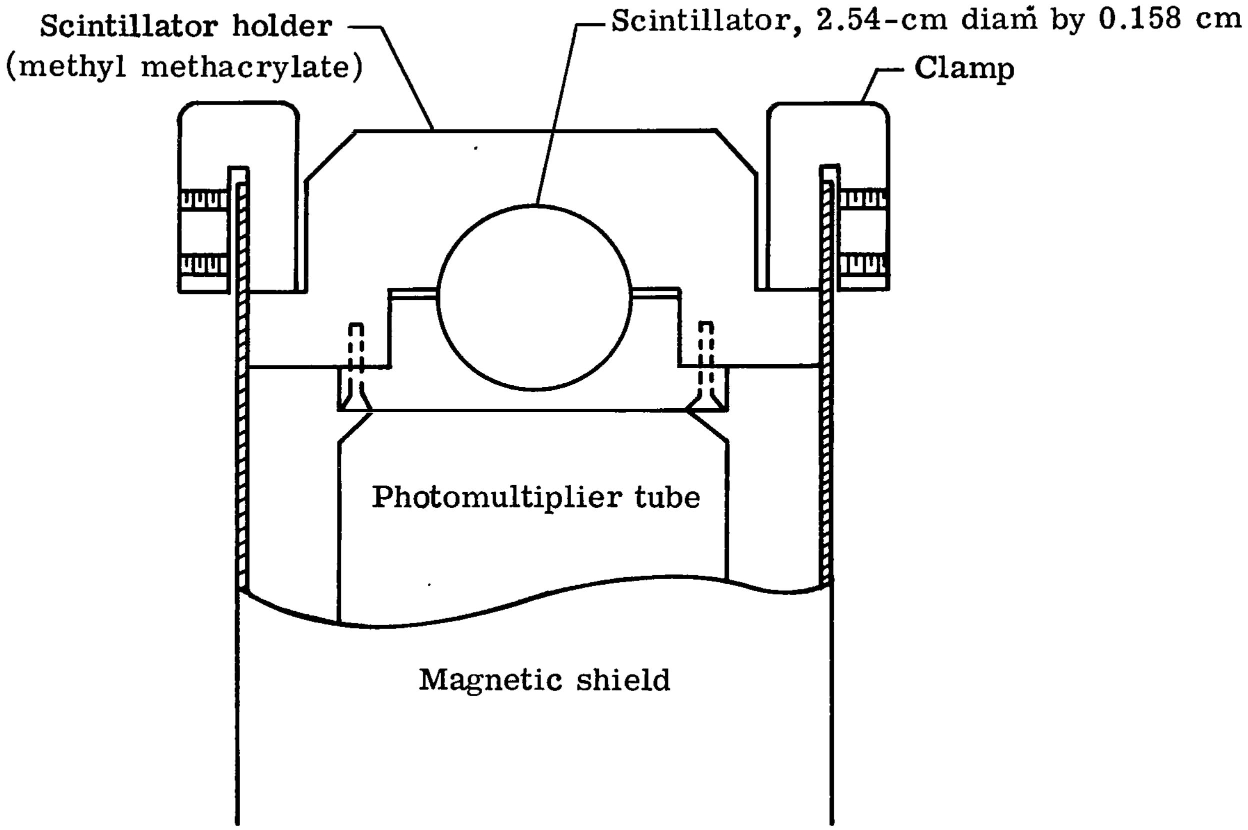

Full scale

(b) Detector 2.

Figure 2.— Continued.

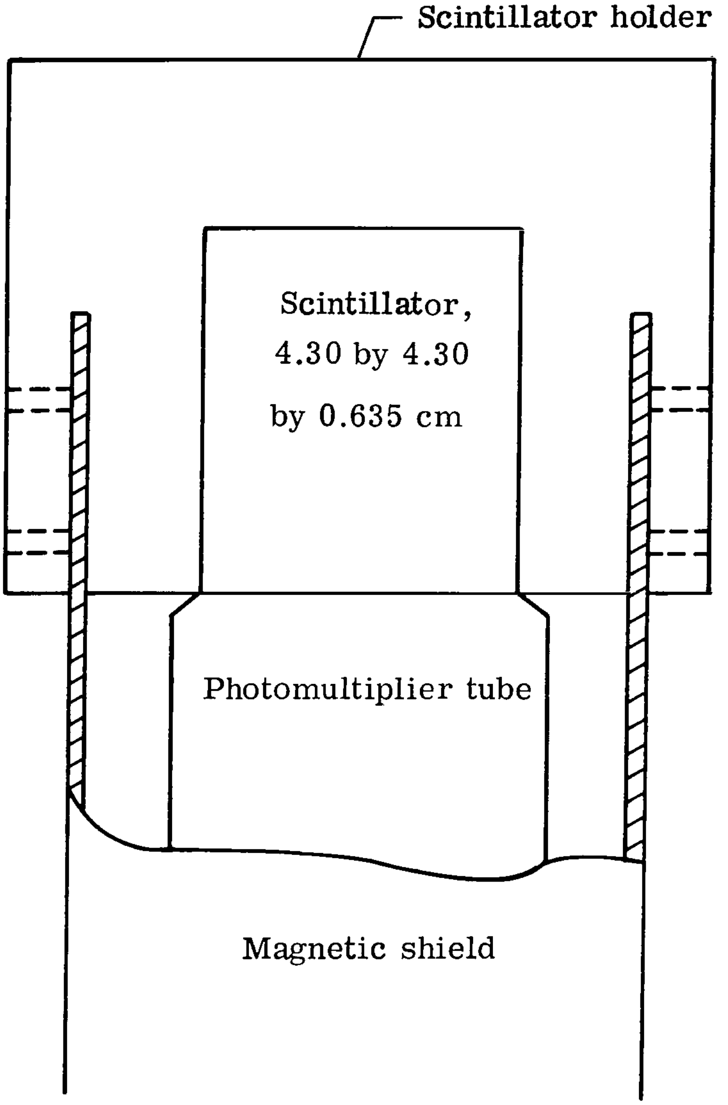

Full scale

(c) Detector 4.

Figure 2.- Concluded.

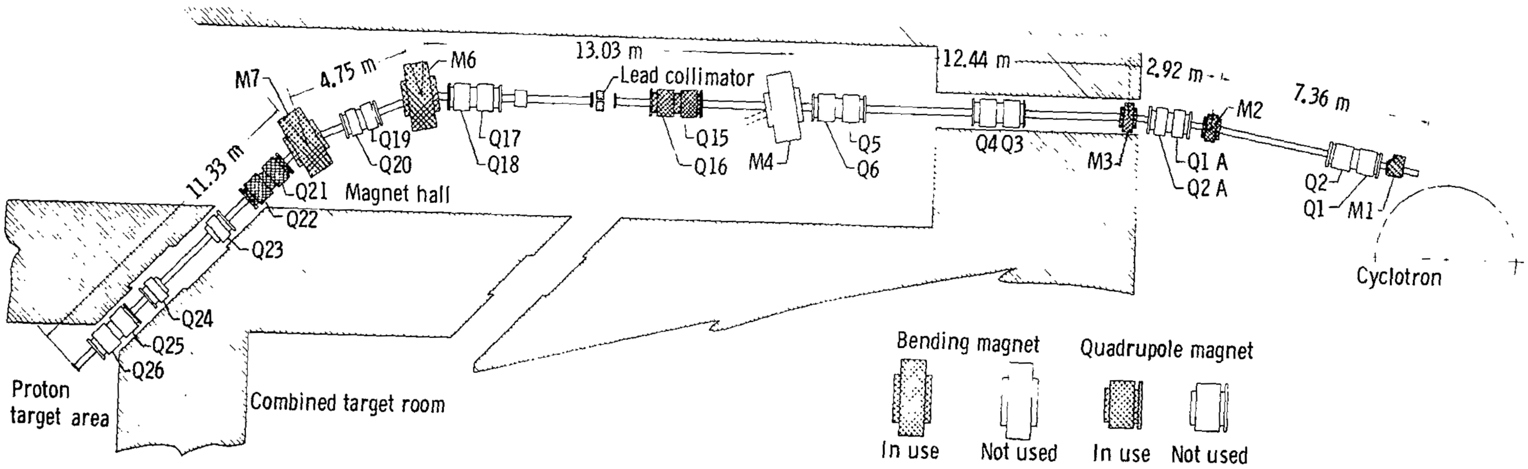

Figure 3.– Beam transport system from cyclotron to proton target area.

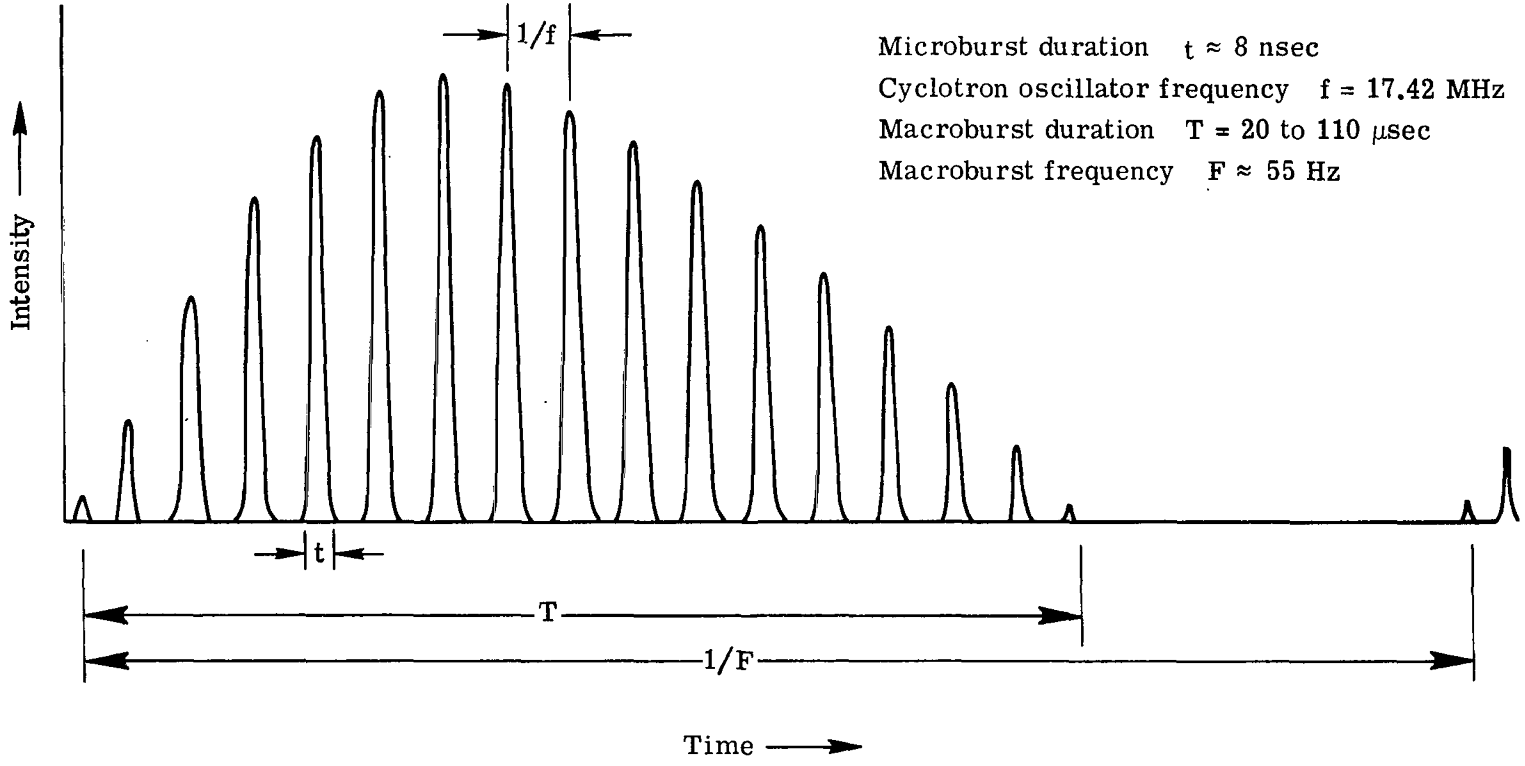

Figure 4.— Distribution of intensity of proton beam macroburst.

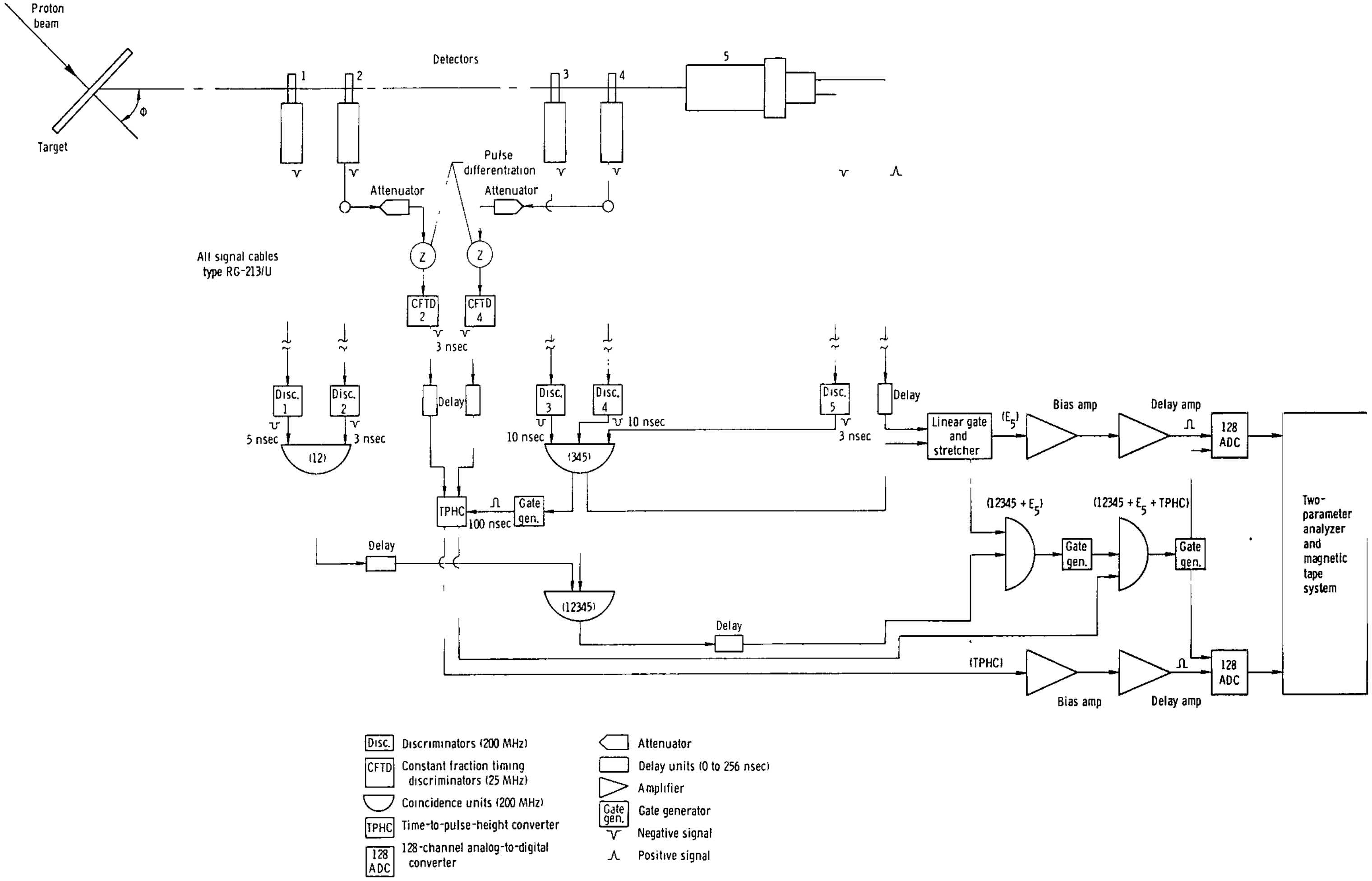

Figure 5.- Schematic of signal processing system.

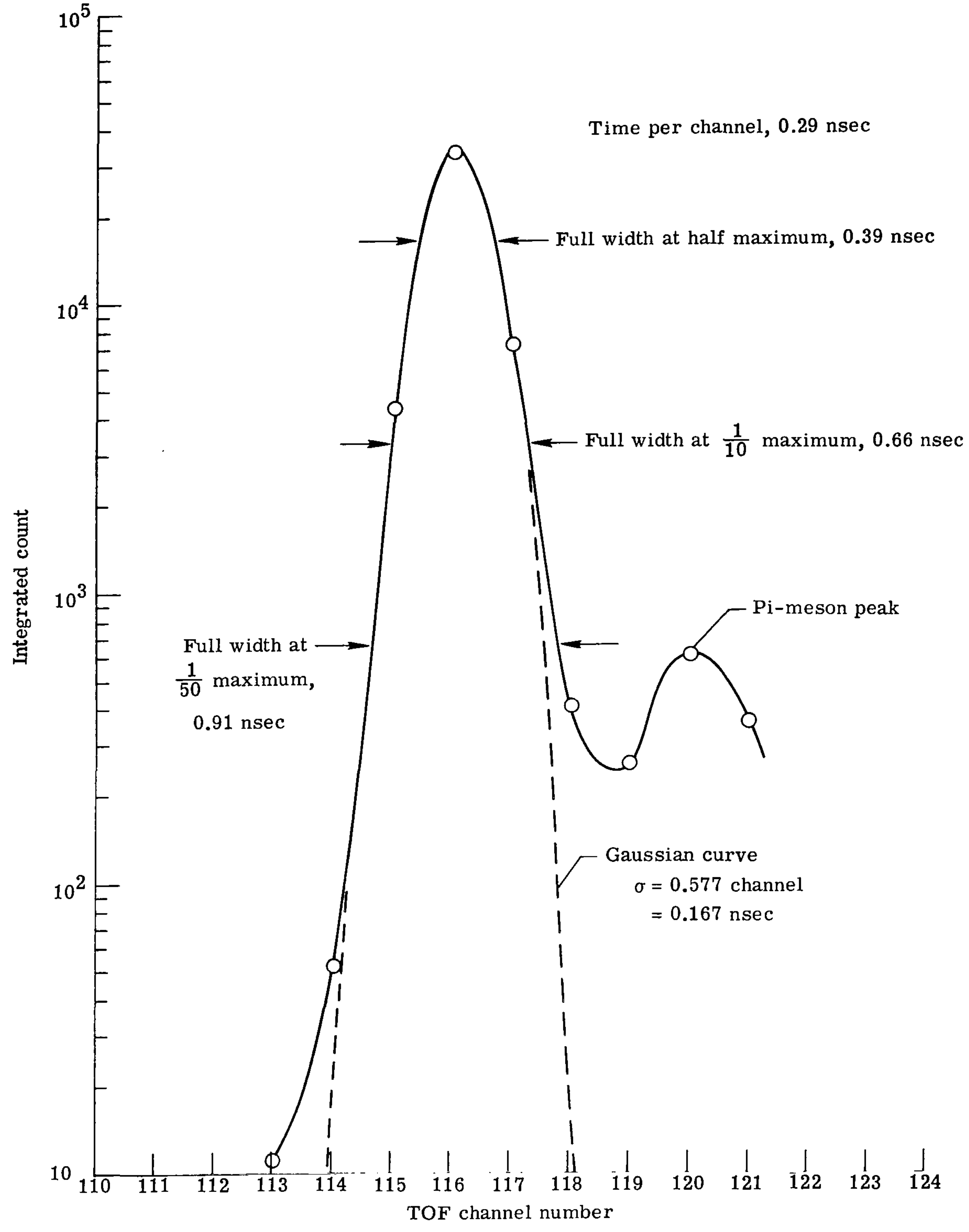

Figure 6.– Time resolution of detection system with 558-MeV incident protons.

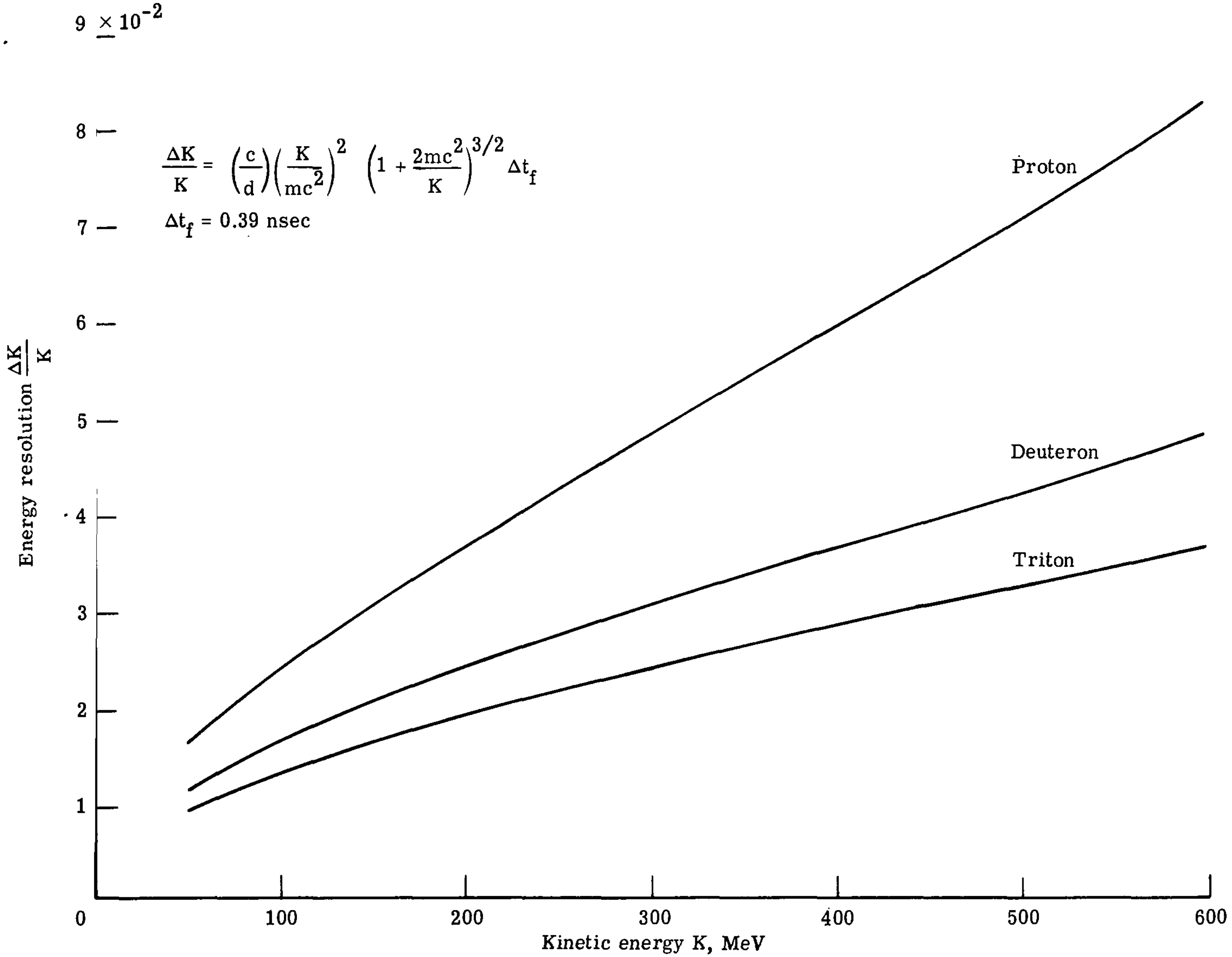

Figure 7.– Time-of-flight energy resolution for protons, deuterons, and tritons calculated for a time resolution of 0.39 nsec.

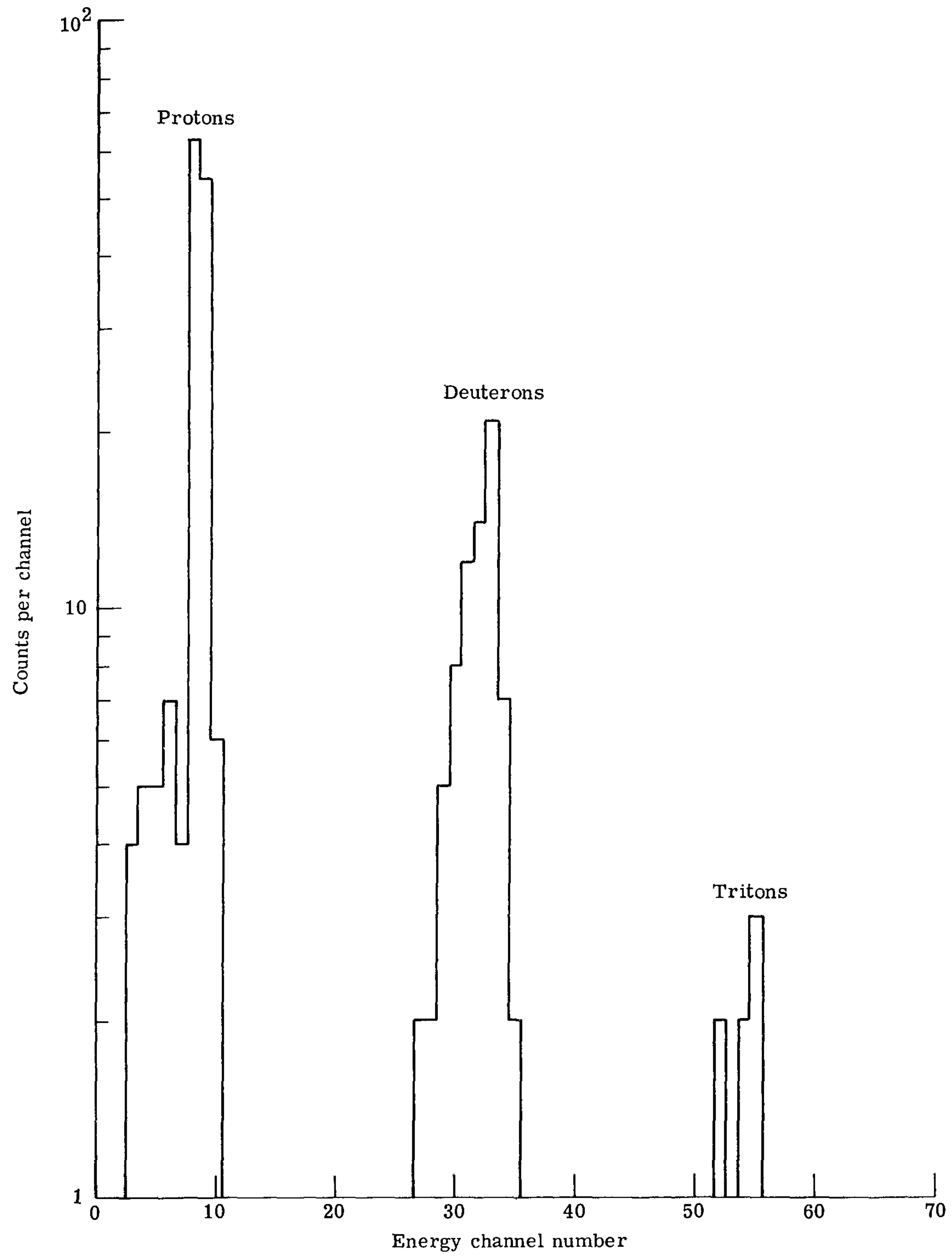

(a) 56 ± 0.8 MeV protons, 112 ± 1.6 MeV deuterons, and 168 ± 2.4 MeV tritons.

Figure 8.— Raw response of detector 5 to protons, deuterons, and tritons of varying energies.

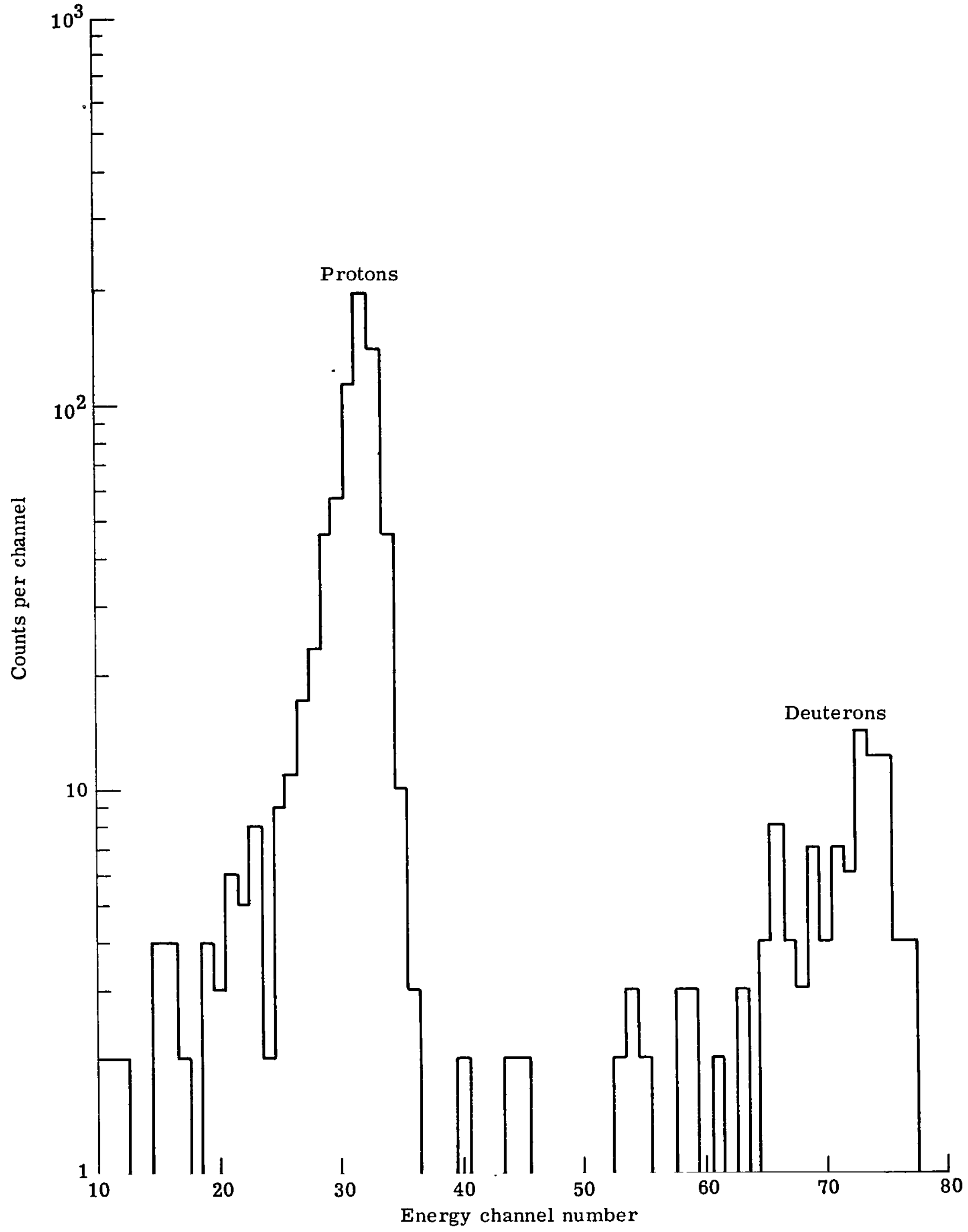

(b) 100 ± 1.9 MeV protons and 200 ± 3.9 MeV deuterons.

Figure 8.— Continued.

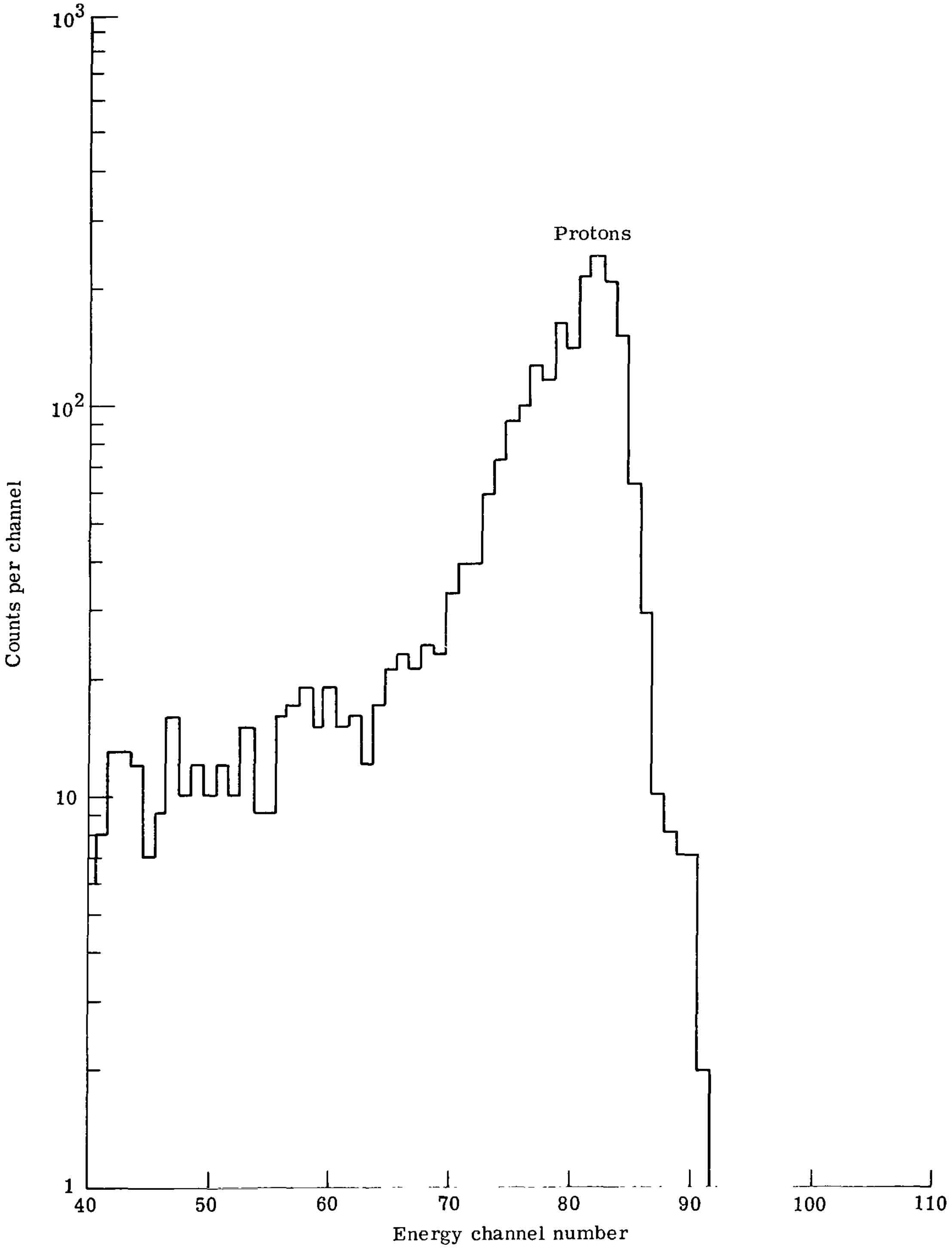

(c) 200 ± 5.9 MeV protons.

Figure 8.– Continued.

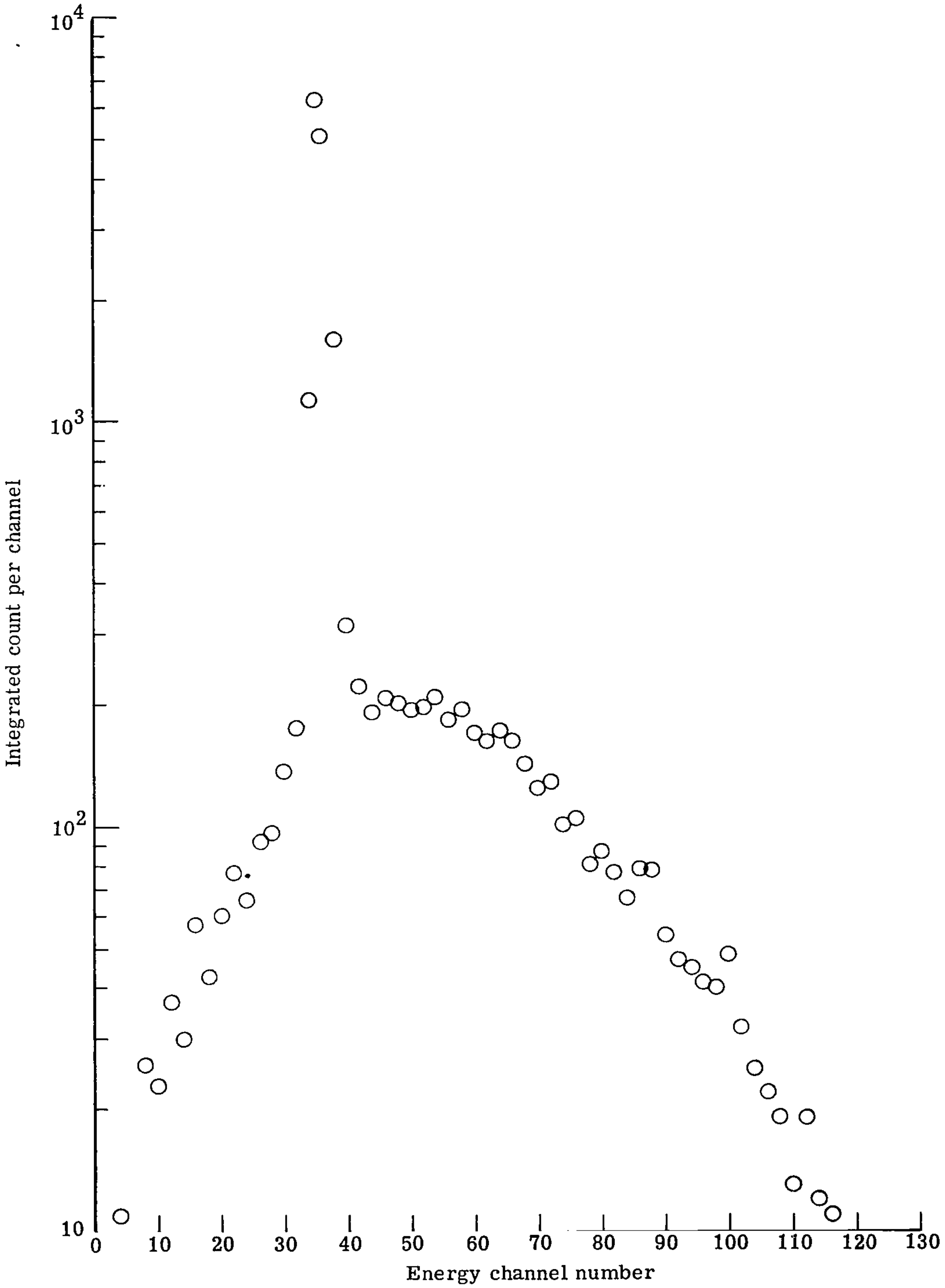

(d) 558-MeV protons.

Figure 8.— Concluded.

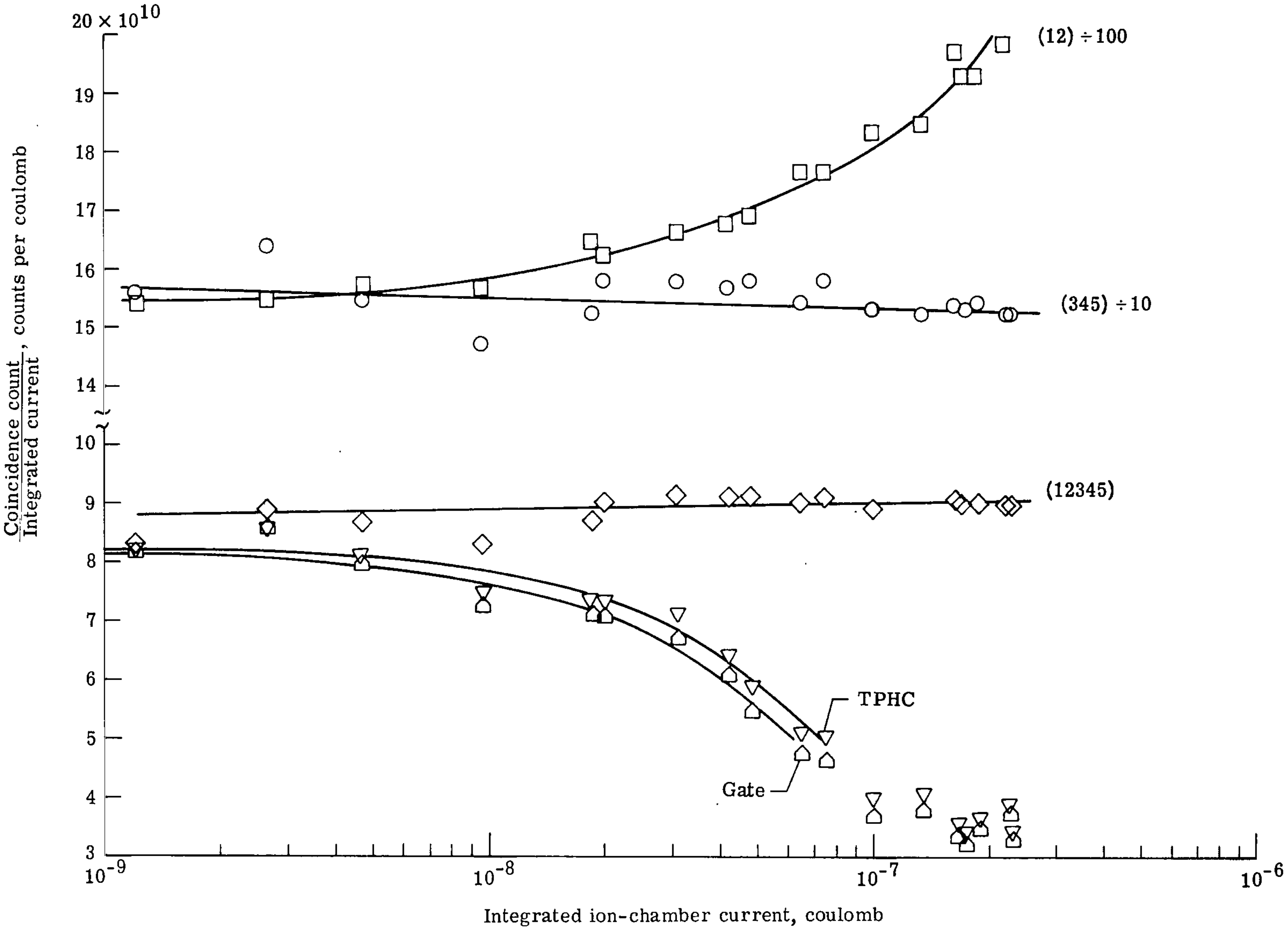

(a) Angle of scatter, 10°; integration time, 72 sec; target, 0.635-cm-thick aluminum.

Figure 9.— Ratio of coincidence count to integrated beam current.

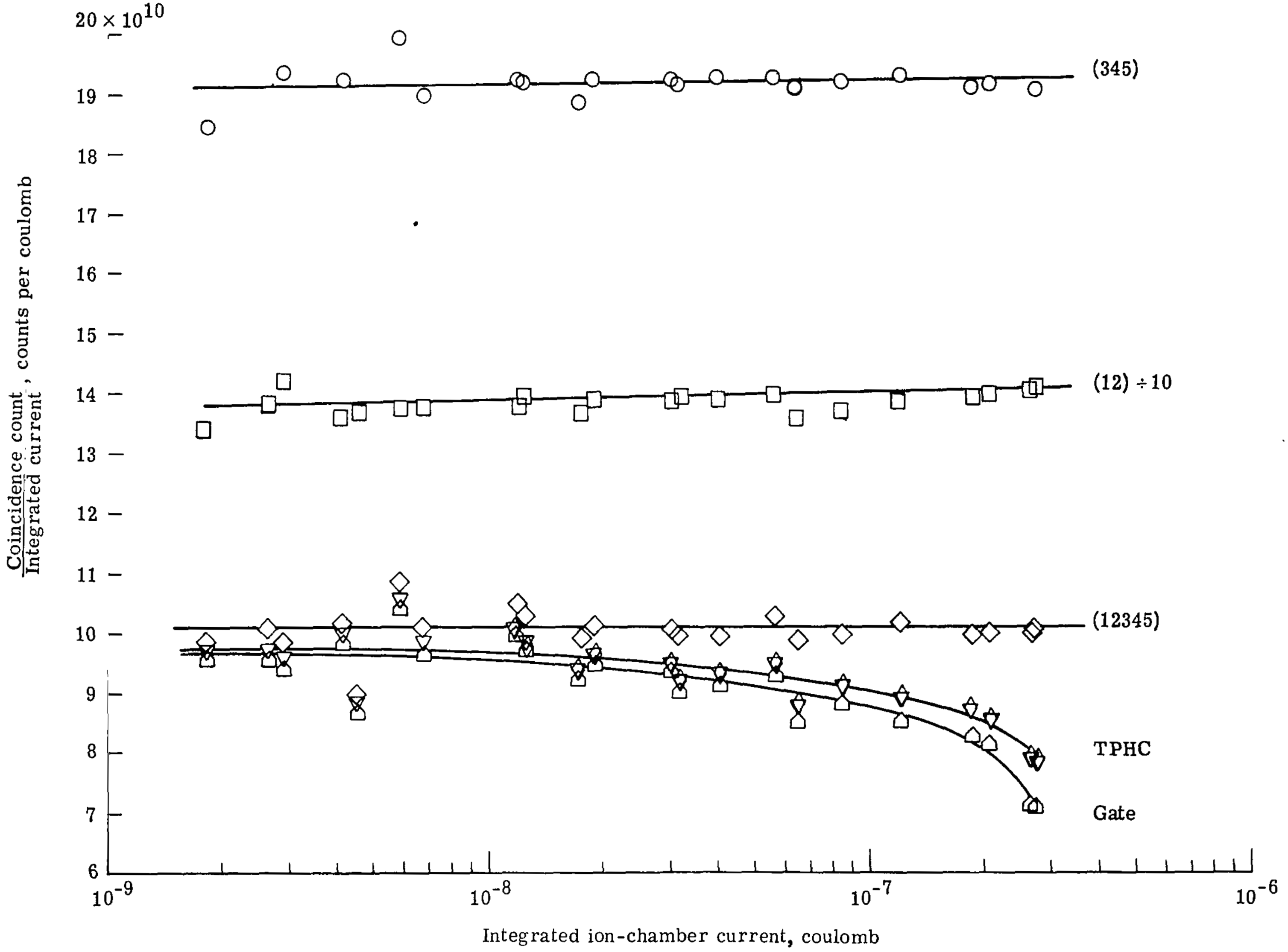

(b) Angle of scatter, 20°; integration time, 60 sec; target, 1.2-cm-thick lead.

Figure 9.– Concluded.

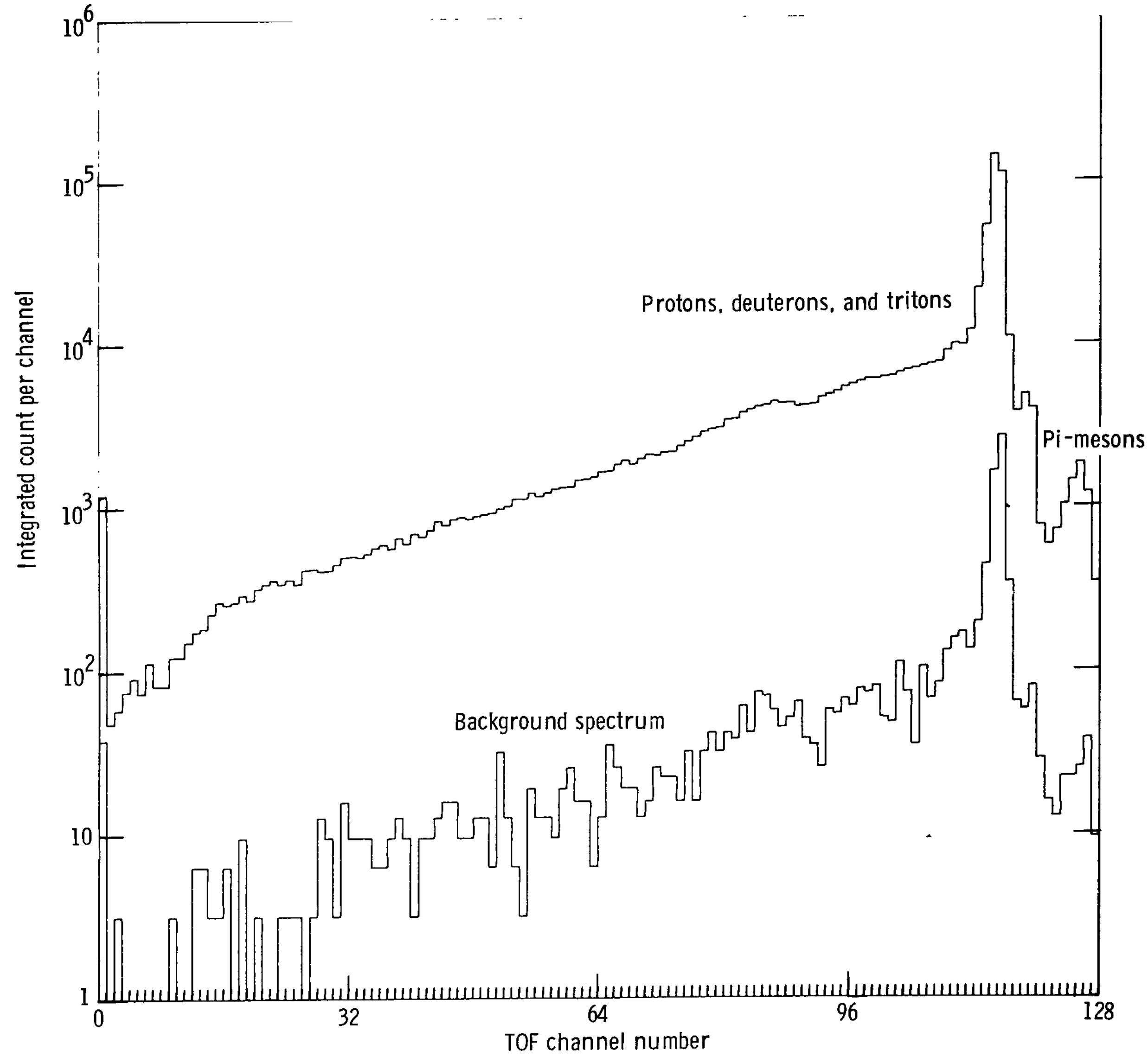

(a) Angle of scatter, 10°; iron target, 3.768 g/cm^2 thick.

Figure 10.— Comparison of integrated raw data spectra from targets with background spectra.

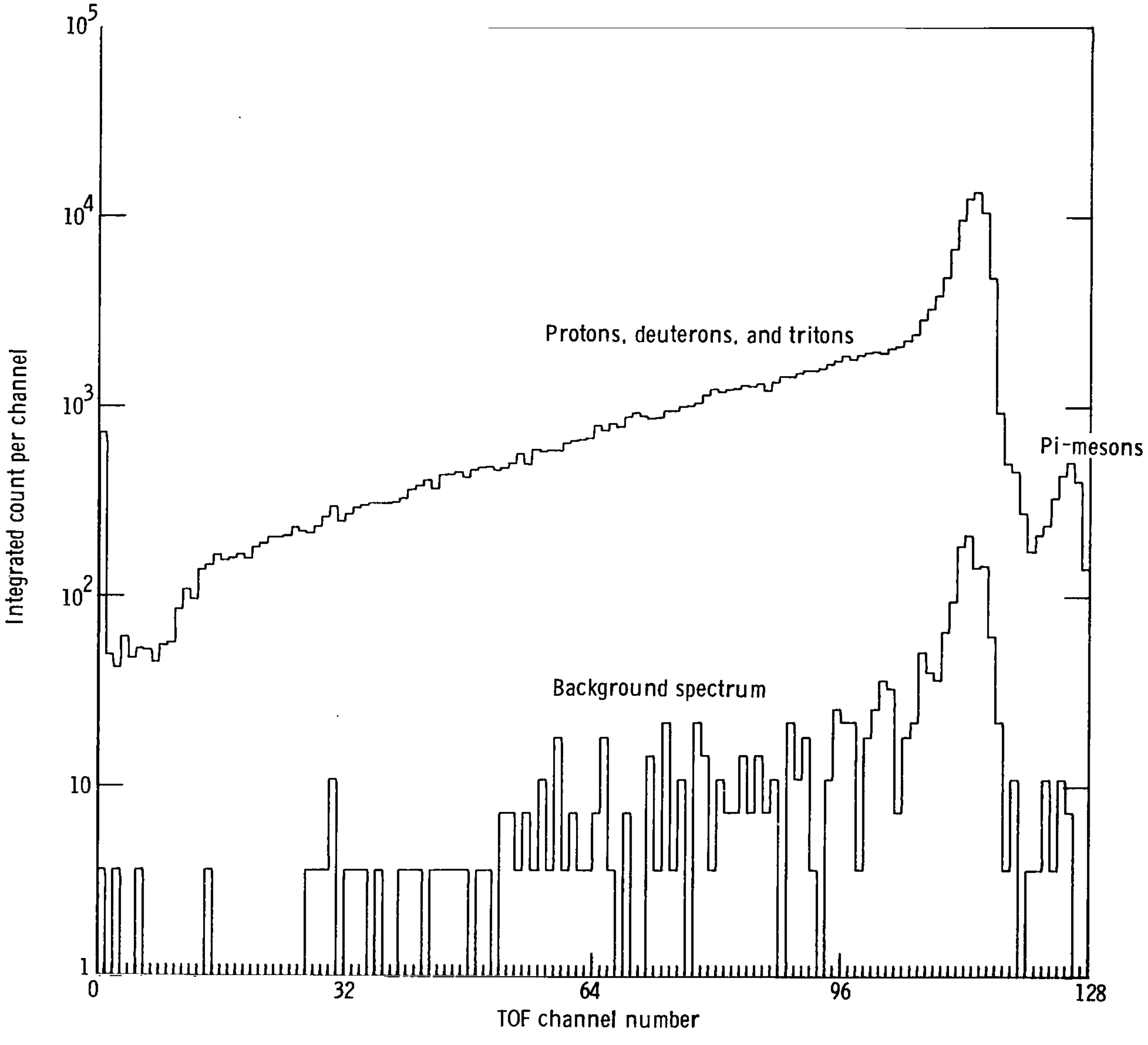

(b) Angle of scatter, 20°; lead target, 3.912 g/cm^2 thick.

Figure 10.— Continued.

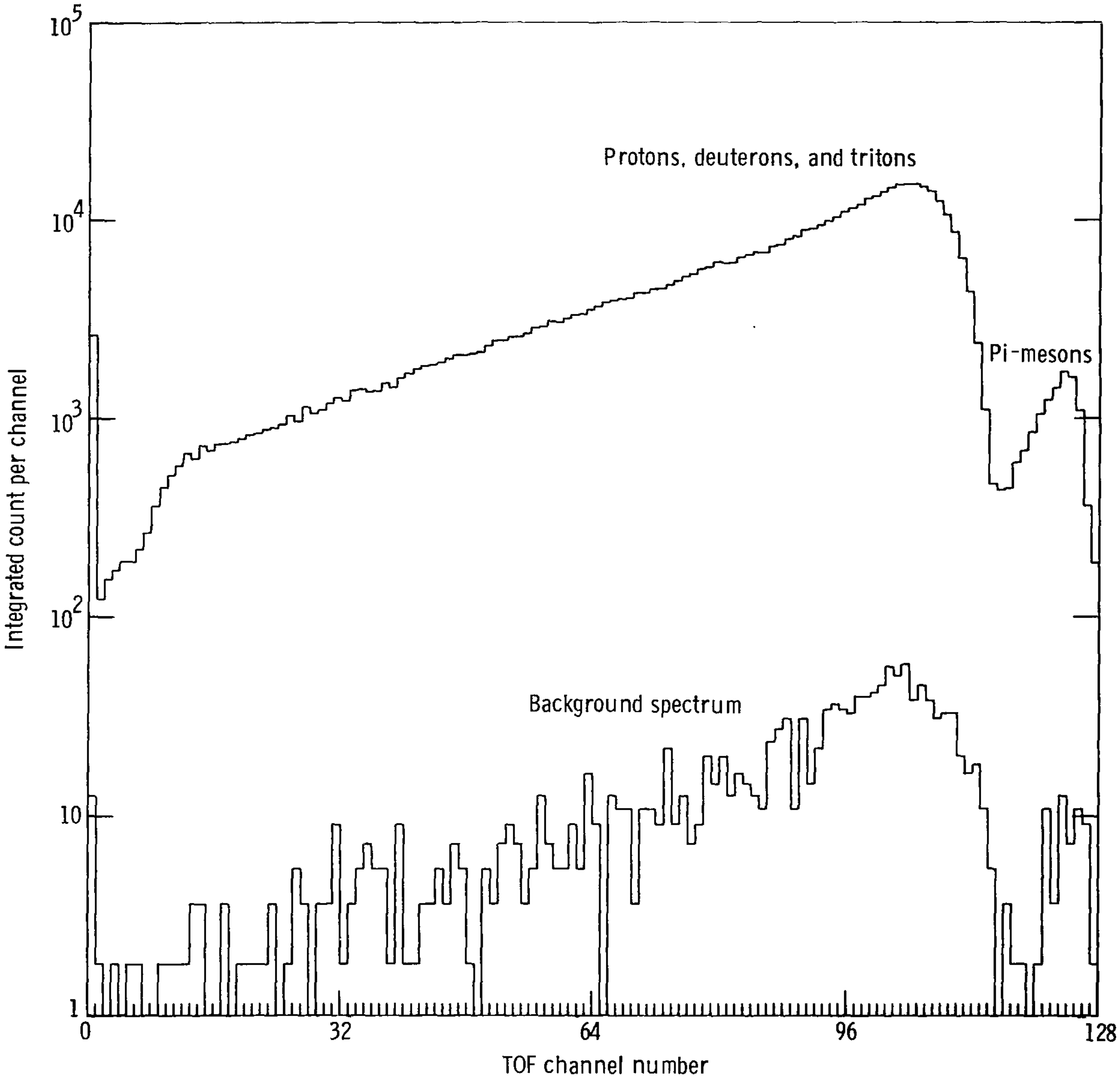

(c) Angle of scatter, 40°; germanium target, 5.263 g/cm^2 thick.

Figure 10.– Continued.

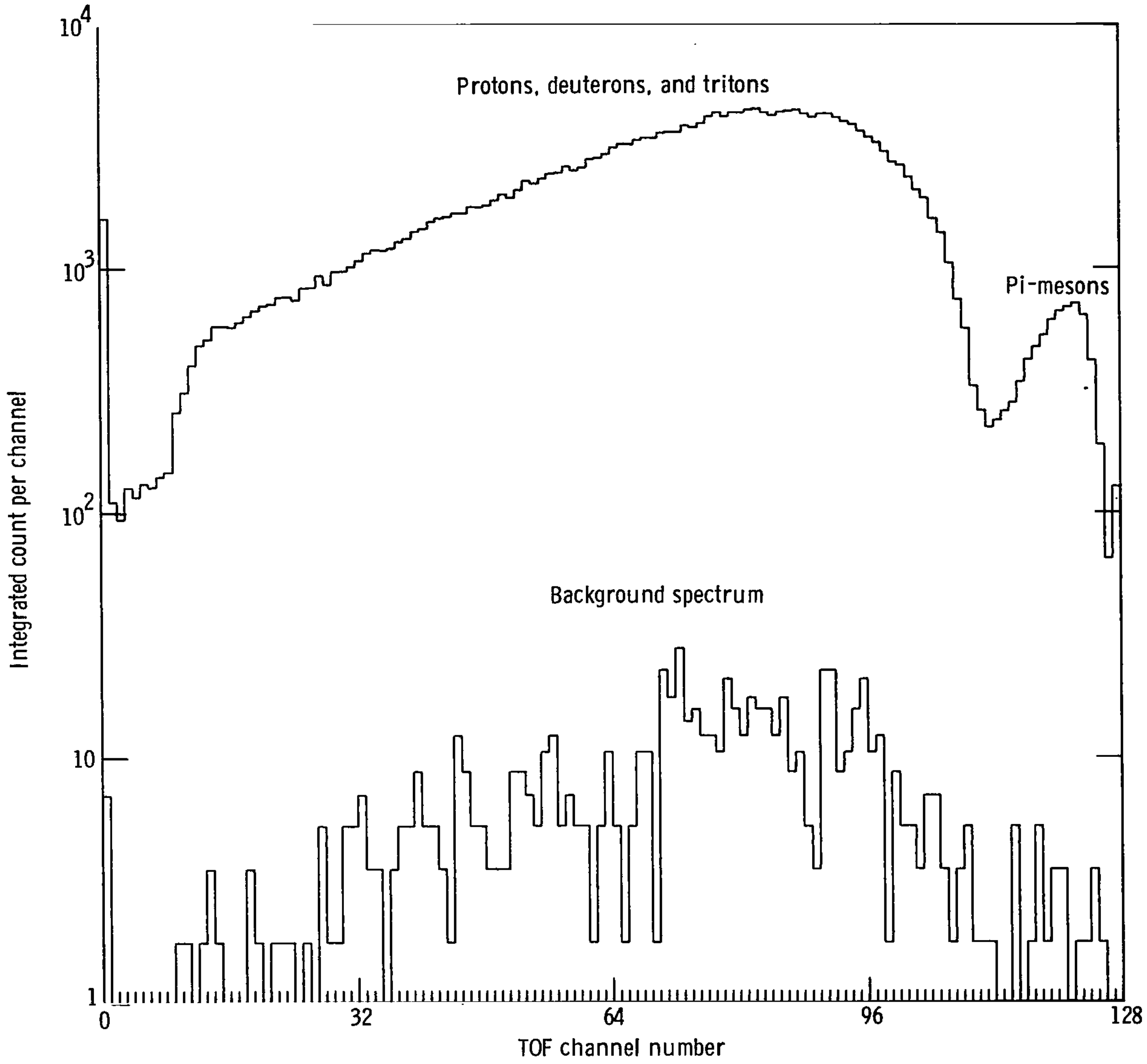

(d) Angle of scatter, 60°; copper target, 2.786 g/cm^2 thick.

Figure 10.— Concluded.

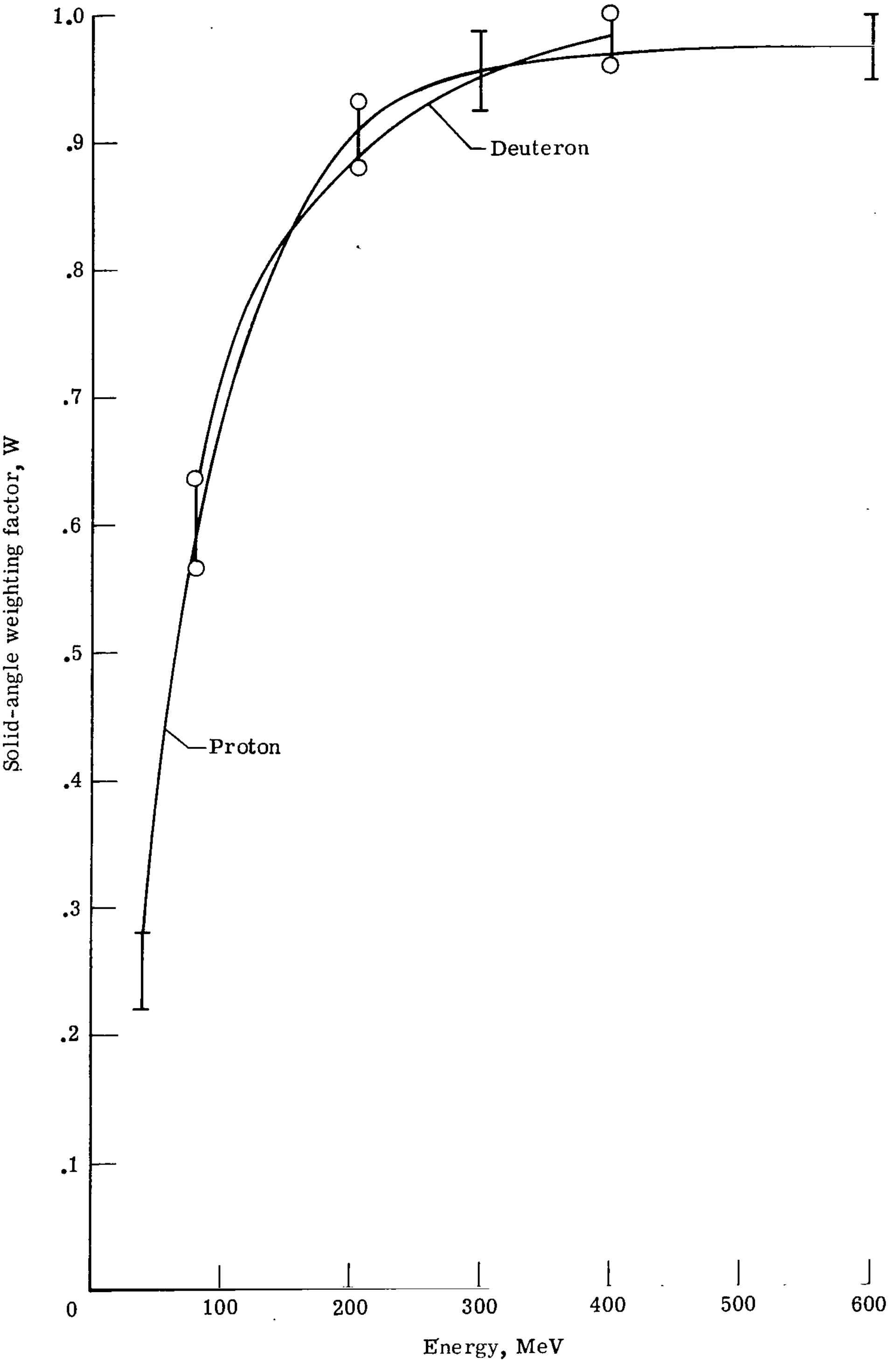

Figure 11.– Variation of the solid-angle weighting factor with energy for protons and deuterons.

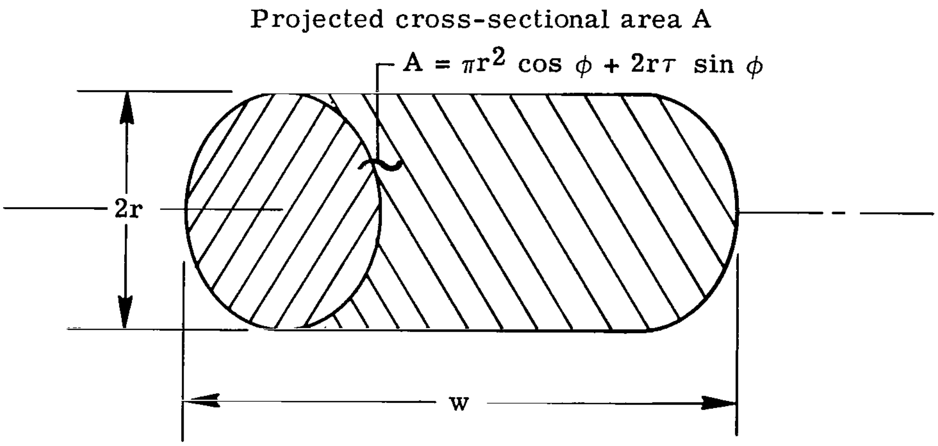

(a) Projected cross-sectional view along detection system center line.

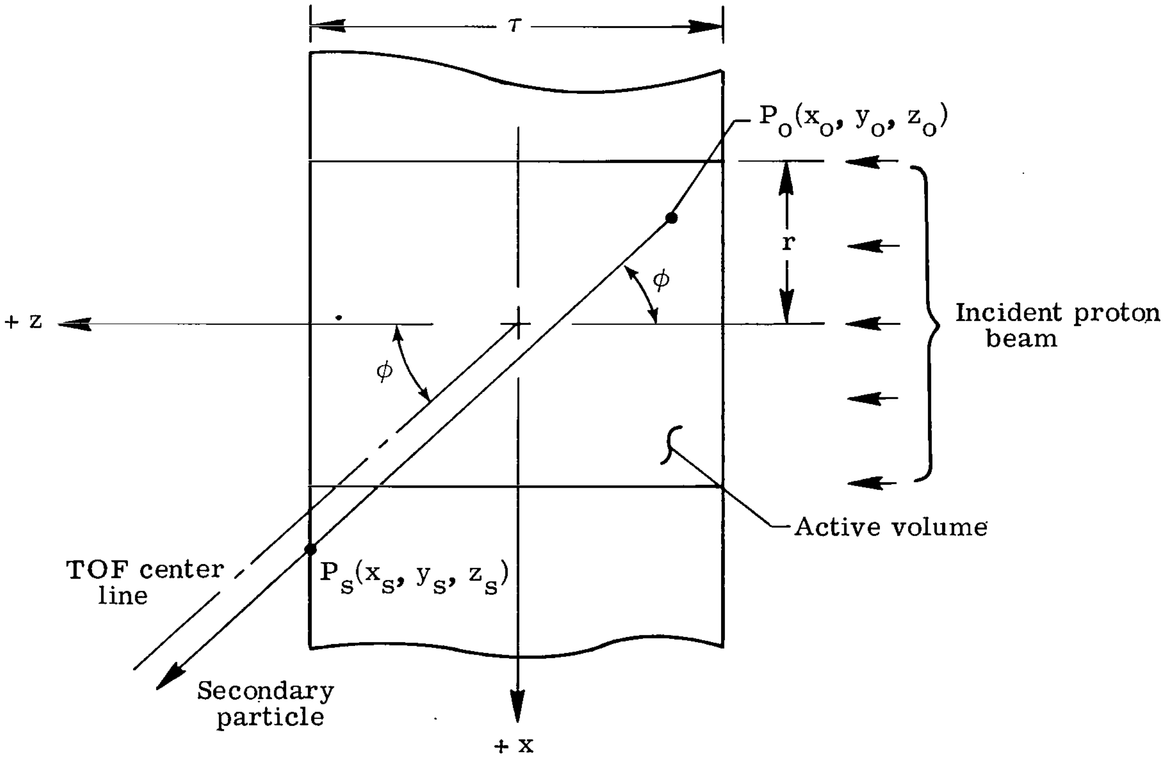

(b) View perpendicular to plane containing beam and detection system center lines.

Figure 12.— Target active volume.

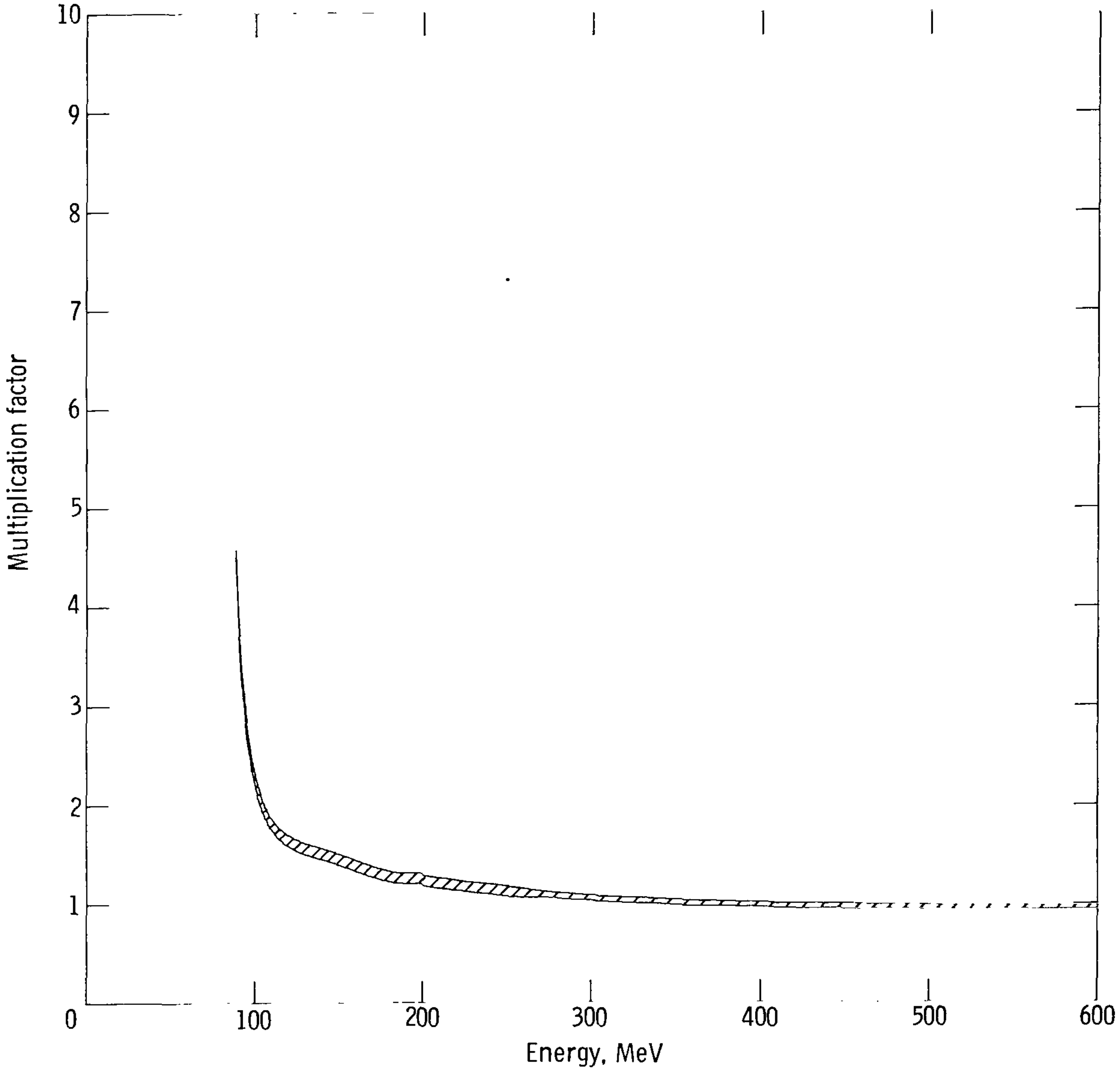

(a) Deuterons.

Figure 13.— Combined raw data multiplication factor at angle of scatter of 20° from 2.35 g/cm^2 thick beryllium target under 558-MeV-proton irradiation.

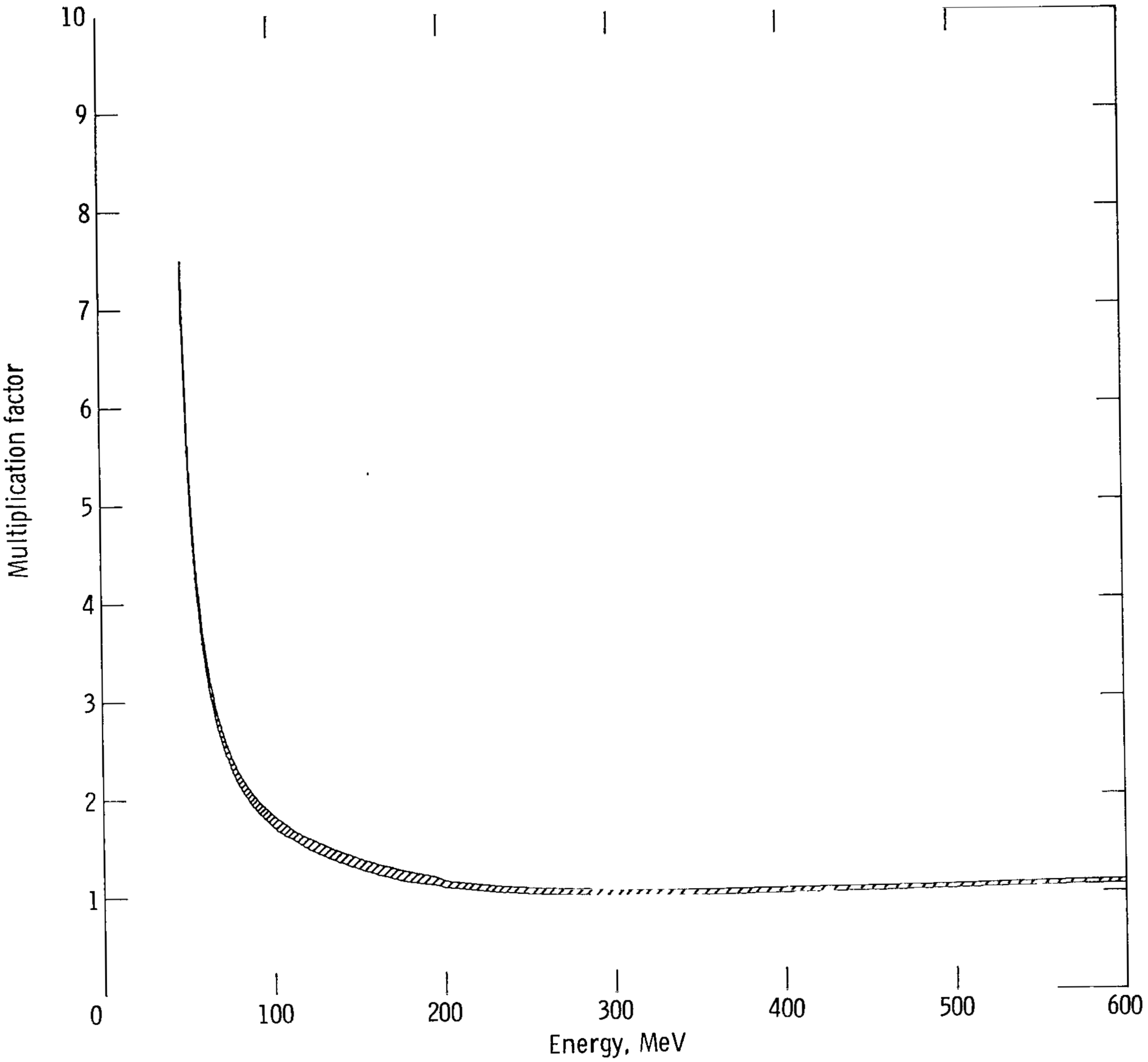

(b) Protons.

Figure 13.– Concluded.

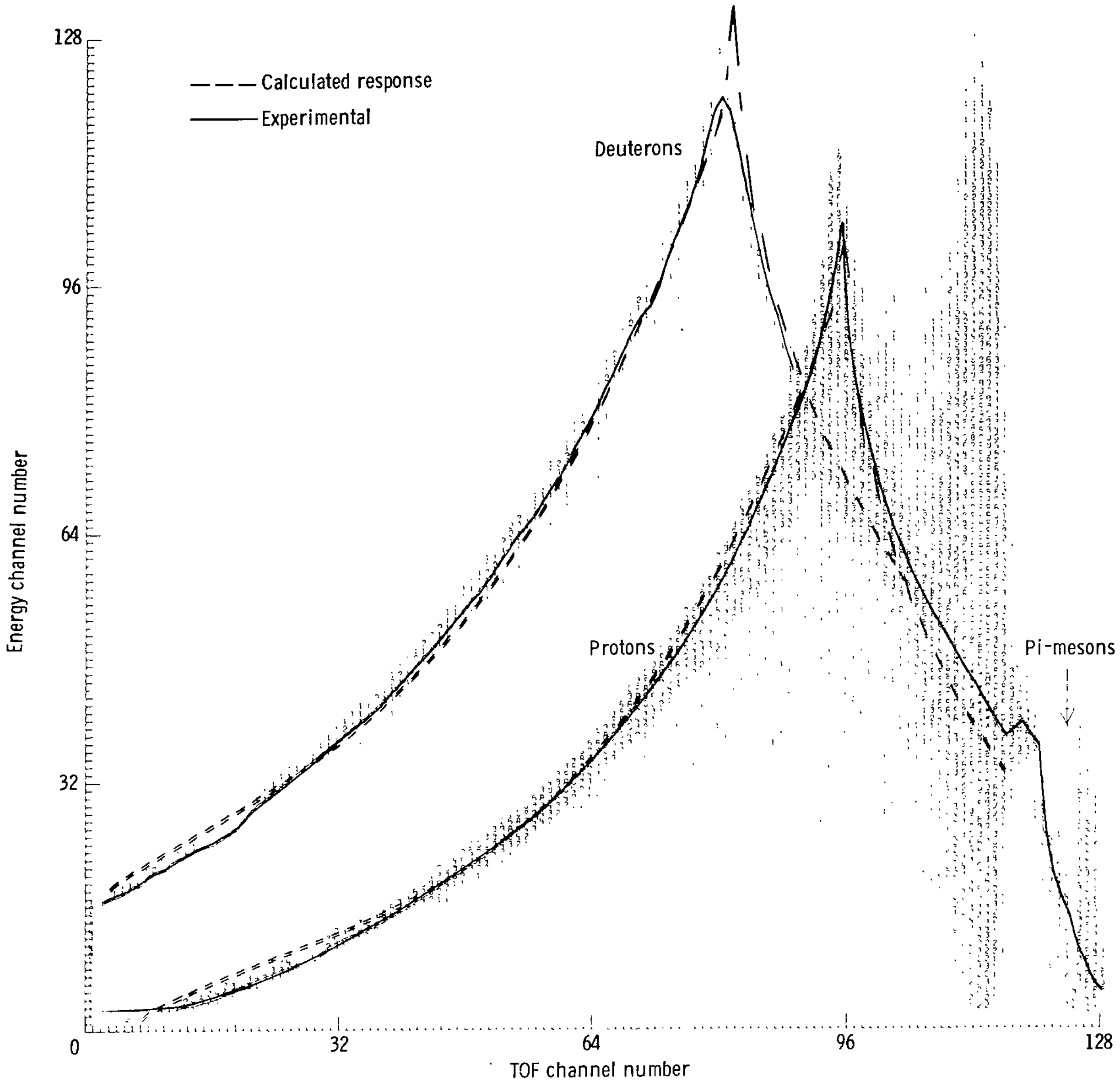

Figure 14.– Raw data contour plot from two-parameter pulse-height analyzer system showing detection system's response to protons, deuterons, and pi-mesons. Solid lines connect maximum values along proton and deuteron distributions. Dashed lines represent calculated response of system.

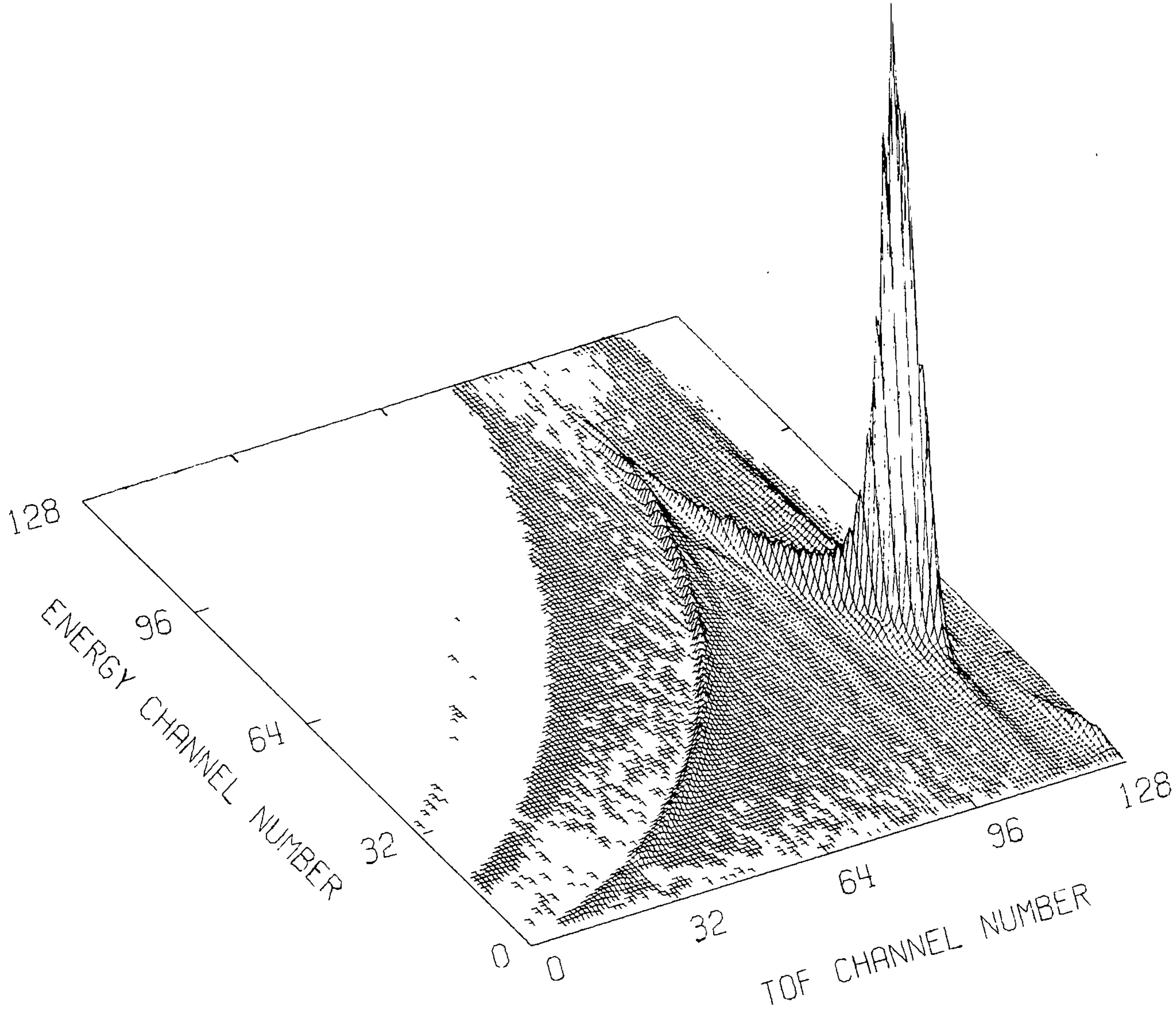

(a) Angle of scatter of 20°.

Figure 15.– Computer-drawn isometric display of raw data from a 2.35 g/cm^2 thick beryllium target.

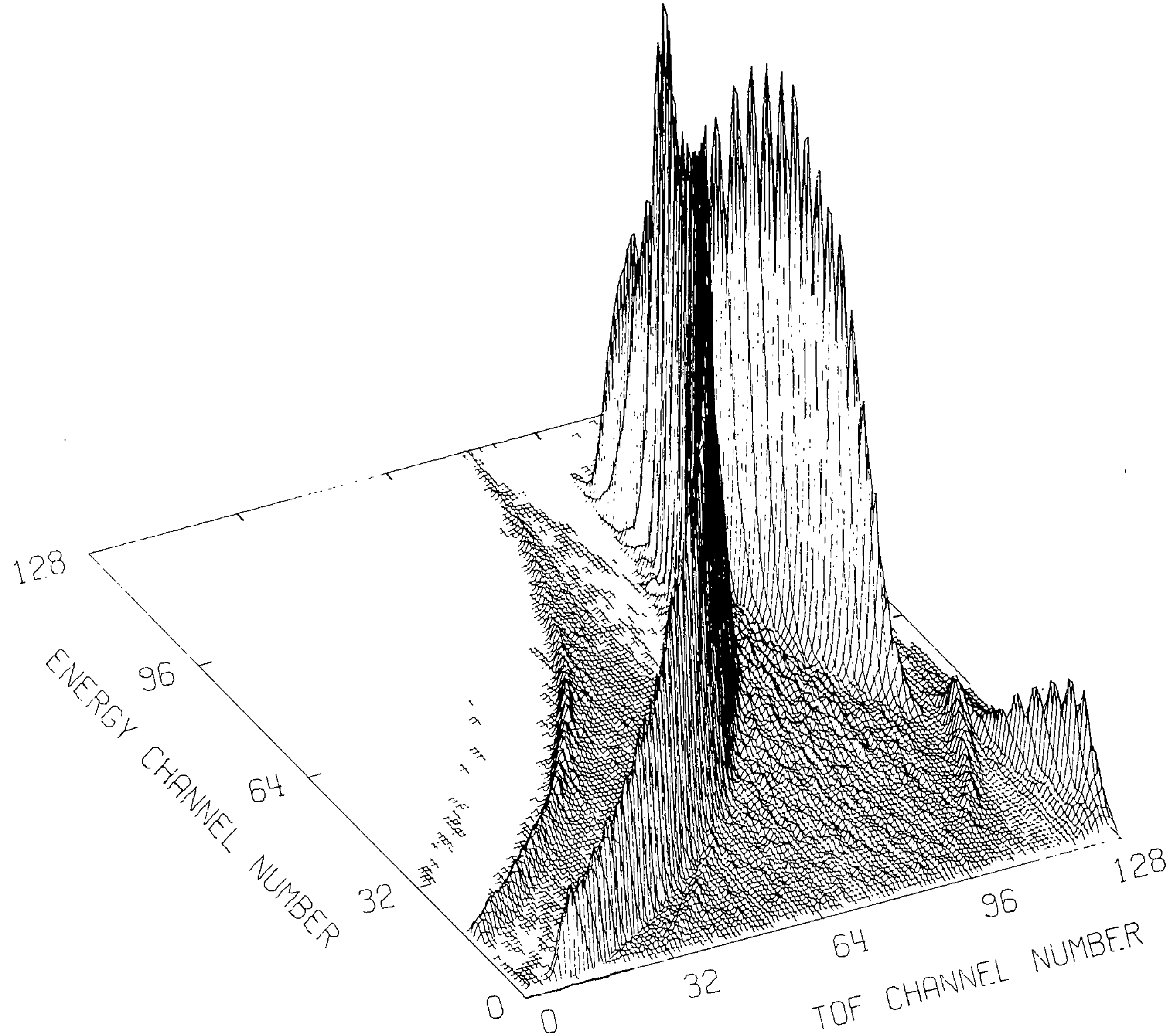

(b) Angle of scatter of 50°.

Figure 15.— Concluded.

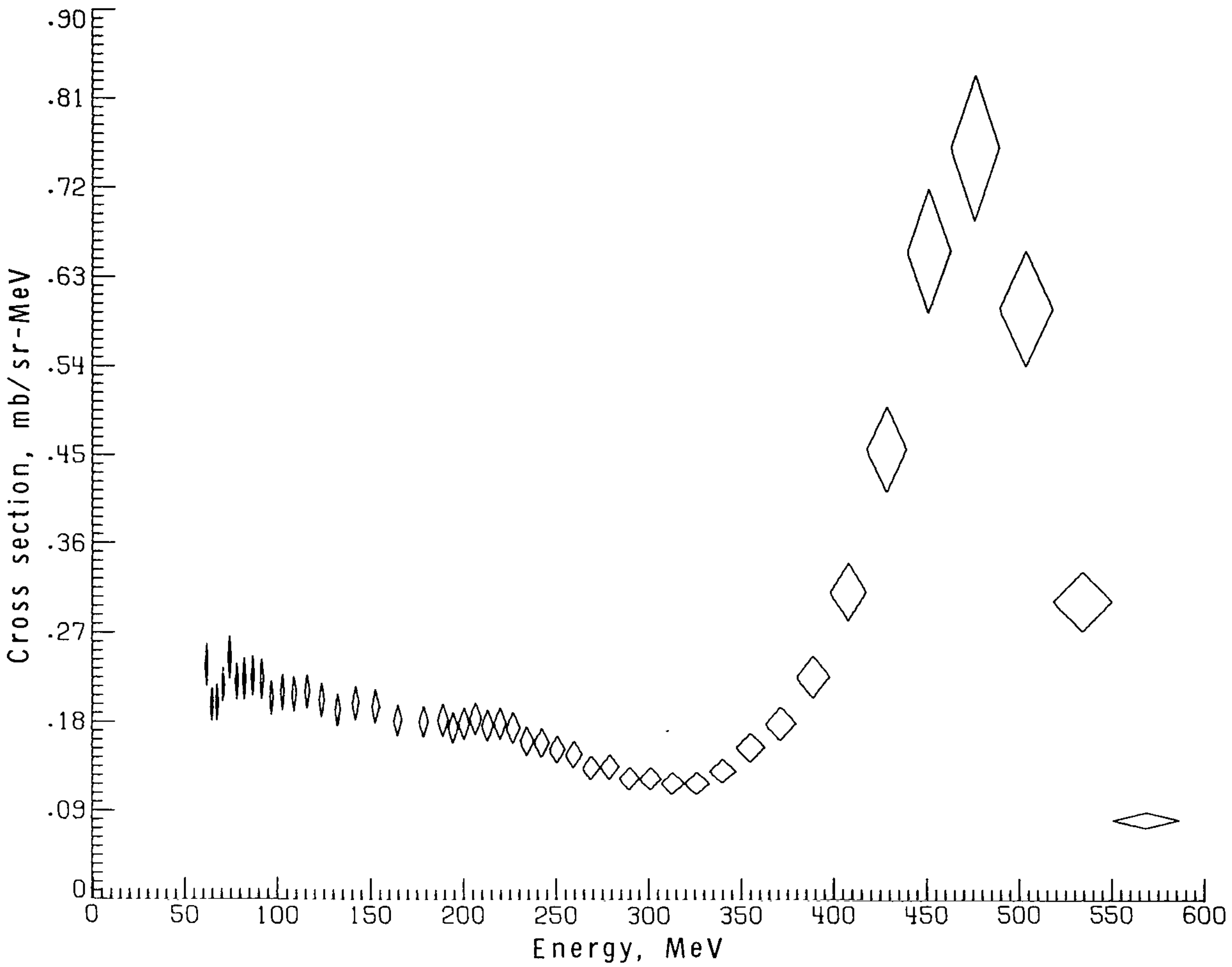

(a) Secondary protons.

Figure 16.– Cross-section spectra at angle of scatter of 20° from 2.35 g/cm^2 thick beryllium target under 558-MeV-proton irradiation.

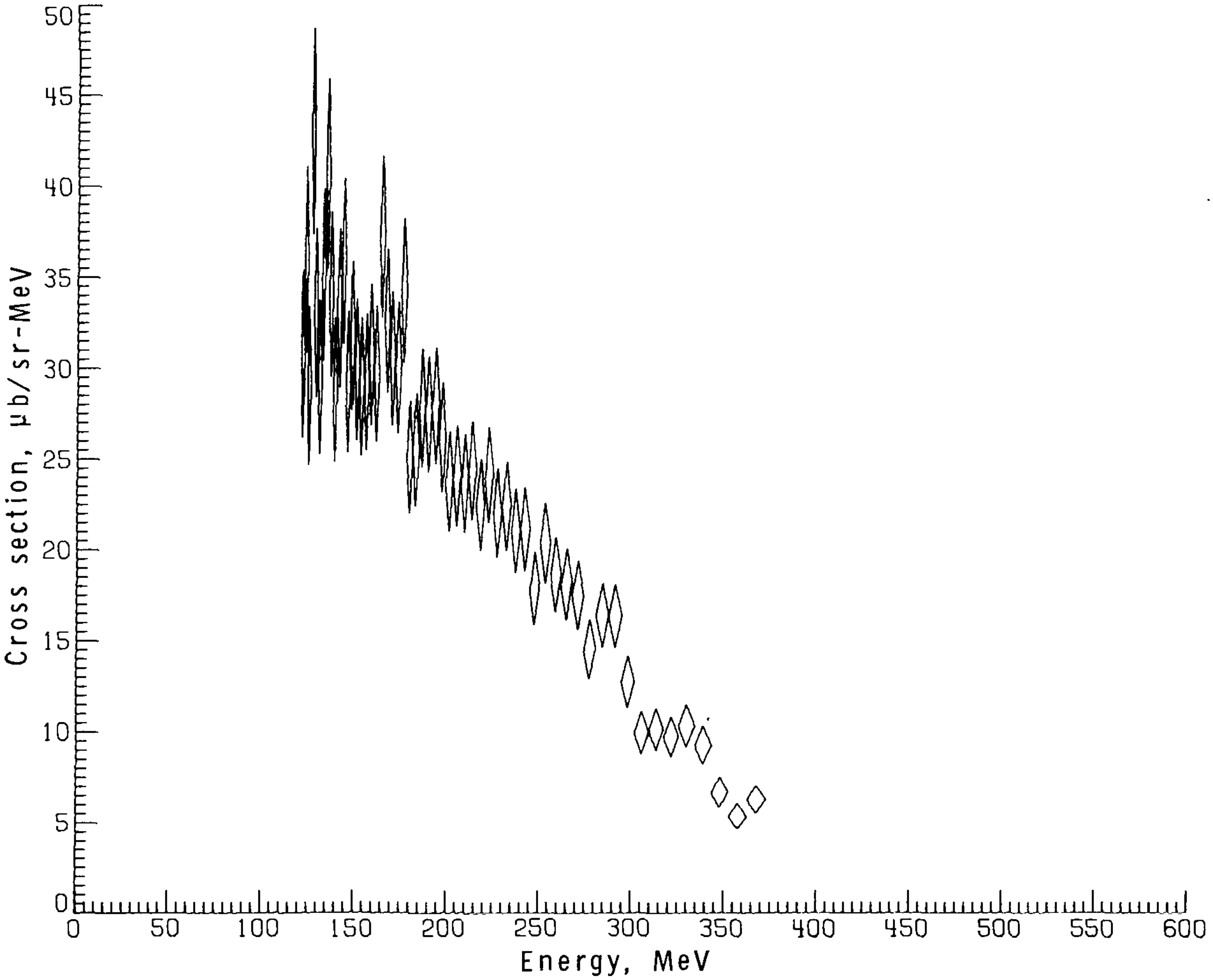

(b) Secondary deuterons.

Figure 16.— Concluded.

NASA-Langley, 1975 L-9941